



Constructing bio-templated 3D porous microtubular C-doped g-C₃N₄ with tunable band structure and enhanced charge carrier separation

Mohamad Azuwa Mohamed^{a,b,*}, M.F. M. Zain^{c,**}, Lorna Jeffery Minggu^a,
 Mohammad B. Kassim^{a,b}, Nor Aishah Saidina Amin^d, W.N. W. Salleh^e,
 Mohd Nur Ikhmal Salehmin^a, Mohd Faizal Md Nasir^a, Zul Adlan Mohd Hir^f

^a Solar Hydrogen Group, Fuel Cell Institute (SELFUEL), Universiti Kebangsaan Malaysia, 43600, UKM, Bangi, Selangor, Malaysia

^b School of Chemical Sciences and Food Technology, Faculty of Science and Technology, Universiti Kebangsaan Malaysia, 43600, UKM, Bangi, Selangor, Malaysia

^c Sustainable Construction Materials and Building Systems (SUCOMBS) Research Group, Faculty of Engineering and Built Environment, Universiti Kebangsaan Malaysia, 43600, Bangi, Malaysia

^d Department of Chemical Engineering, Faculty of Chemical and Energy Engineering, Universiti Teknologi Malaysia, 81310, UTM, Skudai, Johor Baharu, Johor, Malaysia

^e Advanced Membrane Technology Research Centre (AMTEC), Universiti Teknologi Malaysia, 81310, Skudai, Johor Darul Takzim, Malaysia

^f Materials Synthesis and Characterization Laboratory, Institute of Advanced Technology, Universiti Putra Malaysia, 43400, Serdang, Selangor, Malaysia

ARTICLE INFO

Keywords:

g-C₃N₄
 3D micro-tubular structure
 Doping
 Kapok fibre
 Charge separation

ABSTRACT

For the first time, the bio-templated porous microtubular C-doped (BTPMC) g-C₃N₄ with tunable band structure was successfully prepared by simple thermal condensation approach using urea as precursors and kapok fibre which provides a dual function as a bio-templates and in-situ carbon dopant. Prior to the thermal condensation process, the impregnation strategies (i.e. direct wet and hydrothermal impregnation) of urea on the treated kapok fibre (t-KF) were compared to obtained well-constructed bio-templated porous microtubular C-doped g-C₃N₄. The details on a physicochemical characteristic of the fabricated samples were comprehensively analyze using X-ray diffraction (XRD), Fourier transform infrared (FTIR), X-ray photoelectron spectroscopy (XPS), Field-emission scanning electron microscopy (FESEM), Transmission electron microscopy (TEM), N₂ adsorption-desorption, Thermogravimetric (TGA), and UV–vis spectroscopy. Our finding indicated that the hydrothermal impregnation strategy resulted in well-constructed microtubular structure and more carbon substitution in sp²-hybridized nitrogen atoms of g-C₃N₄ as compared to the direct wet impregnation. Also, compared to pure g-C₃N₄, the fabricated BTPMC g-C₃N₄ exhibited extended photoresponse from the ultraviolet (UV) to visible and near-infrared regions and narrower bandgap. The bandgap easily tuned with the increased t-KF loading in urea precursor which responsible for in-situ carbon doping. Moreover, as compared to pristine g-C₃N₄, dramatic suppression of charge recombination of the BTPMC g-C₃N₄ was confirmed through photoluminescence, photocurrent response, and electrochemical impedance spectroscopy. The resultants BTPMC g-C₃N₄ possesses more stable structure, promoted charge separation, and suitable energy levels of conduction and valence bands for photocatalysis application.

1. Introduction

Photocatalysis is widely used for hydrogen production, CO₂ photo-reduction well as organic contaminants decomposition. The ideal photocatalytic material should possess a moderate band gap, which absorbs light in the visible range and is efficient in separating, collecting and transporting charges for the chemical processes. Recently, graphitic carbon nitride (g-C₃N₄) has emerged as an innovative

photocatalyst with tunable band gaps of 1.8–2.7 eV that allow the harvesting of visible light ranging from 460 to 698 nm (potentially utilise 13–49% of solar energy, though the photocatalytic activity may reduce at a longer wavelength). The g-C₃N₄ possesses a stacked 2D structure, which could regard as a nitrogen heteroatom-substituted graphite framework consisting of p-conjugated graphitic planes formed via sp² hybridisation of carbon and nitrogen atoms. This material is made from earth-abundant, inexpensive C and N containing precursors

* Corresponding author at: Solar Hydrogen Group, Fuel Cell Institute (SELFUEL), Universiti Kebangsaan Malaysia, 43600, UKM, Bangi, Selangor, Malaysia & School of Chemical Sciences and Food Technology, Faculty of Science and Technology, Universiti Kebangsaan Malaysia, 43600, UKM, Bangi, Selangor, Malaysia.

** Corresponding author at: Sustainable Construction Materials and Building Systems (SUCOMBS) Research Group, Faculty of Engineering and Built Environment, Universiti Kebangsaan Malaysia, 43600, Bangi, Malaysia.

E-mail addresses: mazuwa@ukm.edu.my (M.A. Mohamed), fauzizain@ukm.edu.my (M.F. M. Zain).

<https://doi.org/10.1016/j.apcatb.2018.05.037>

Received 23 March 2018; Received in revised form 9 May 2018; Accepted 12 May 2018

Available online 15 May 2018

0926-3373/ © 2018 Elsevier B.V. All rights reserved.

(e.g., urea, melamine), is biocompatible with no reported toxicity, is resistant to photo-corrosion, and remains chemically stable in harsh environments.

However, pure g-C₃N₄ suffers from the insufficient sunlight absorption, low surface area and the fast recombination of photo-induced electron-hole pairs, resulting in low photocatalytic activity. To substantially utilise the solar energy, it is far from satisfactory to make photocatalysts only respond to UV (~ 5%) and visible light (~ 43%), with the near-infrared (NIR) photons waste, which makes up a significant portion ~ 52% of the whole solar spectrum. To date, only a few studies report on NIR photocatalysis [1].

Element doping is known to be an efficient method to tune the unique electronic structure and the band gap of g-C₃N₄, which considerably broaden the light responsive range and enhance the charge separation [2]. Up until today, there are several elements has been used as dopants in g-C₃N₄ which differentiated into metal (K, Na, Fe, Cu, Ce, Co, Eu, Mo, W, Y, Zr) and non-metal (P, S, O, C, N, B, F, I, Br) dopants [2]. In comparison with a metal dopant, the non-metal dopant is relatively low-cost and enhanced the mobility of photo-induced charge carriers. In contra, the metal dopants or nanoparticles are more expensive (e.g., noble metal loading), and they may leach or deactivated in complex aquatic chemistries (e.g., metals fouled by natural organic matter, NOM, or sulfide) [3]. In the present study, the selection of C as dopants elements was due to its earth-abundant, low-cost, non-toxic dopants as compared to other non-metal dopants. Furthermore, the utilising C as the dopant material in g-C₃N₄ are due to its comparable atomic size with nitrogen, small ionisation energy, eco-friendly, higher stability and simple synthesis methods [4]. Besides, the density functional theory (DFT) simulations indicated that C-doped g-C₃N₄ showed a thermodynamically stable structure, promoted charge separation, and suitable energy levels of conduction and valence bands for photocatalytic oxidation, compared to phosphorous-doped g-C₃N₄ [3].

The previous study utilised barbituric acid was used as a source of carbon or doping because it can be incorporated into the supramolecular complex of melamine and cyanuric acid via hydrogen bonding or electrostatic interactions to promote efficient doping [3,5]. Later, the porous carbon-doped g-C₃N₄ nanosheets photocatalysts (NSs-APAM) were synthesised using anionic polyacrylamide (APAM) as the intercalator and carbon source via the thermal treatment method. In the same year of 2017, the post granulation thermal oxidation treatment resulted in in-situ doping of carbon leading to improved photophysical properties compared to pristine g-C₃N₄. Also, the self-carbon doping also has been reported by the previous study using melamine as precursor [6,7].

Recently, increasing number of researchers from China's researcher were emphasising the utilisation of kapok fibre as bio-templates in metal oxides preparation for various application. For instance, the three-dimensional (3D) carbonised kapok fibre/nickel oxide, manganese oxide and cobalt-nickel binary oxide hybrids for high-performance electrode materials of supercapacitors [8–11]. Moreover, the kapok fibre also has been used in the preparation of the 3D hierarchic heterojunction photocatalysts assembled from interlinked MoS₂/CoAl-LDH (CoAl-layered double hydroxide)@carbon micron fibre for visible-light degradation of Congo Red [12]. On the other hand, the SnO₂ hollow fibre for application in dye-sensitised solar cells also has successfully prepared by researchers from South Korea using kapok as a bio-templates [13]. However, to the best of our knowledge, it is tough to find the utilisation of bio-templated in synthesis carbon doped g-C₃N₄ in the open literature. Most of the time, C-doped photocatalyst prepared via the bio-templated synthesis was only focusing on the metal oxides such as TiO₂, MnO, and ZnO [14–19]. On top of that, the utilisation of kapok fibre as bio-templates and in-situ carbon dopant in the preparation of carbon doped g-C₃N₄ is still not yet reported.

Here, for the first time, we reported the facile synthesis of g-C₃N₄ using urea as a precursor and kapok fibre as bio-templates and in-situ carbon dopant sources. Kapok fibre as cellulose-based materials is used

as bio-templates due to its insolubility, which renders them more appropriate for bio-replication than for nanoparticle growth control. The incorporated urea precursor could be bound to the kapok fibre via electrostatic interaction and hydrogen interaction because the electron-rich oxygen atoms of the polar hydroxyl groups of cellulose are expected to interact with the urea in aqueous solution. Our finding indicates that the resultants bio-templated microtubular carbon doped g-C₃N₄ show excellent enhancement in charge carrier separation for high-performance photocatalytic material.

2. Experimental

2.1. Materials

Kapok fibre as bio-template were obtained from Perusahaan Bonda, Kuala Kangsar, Perak, Malaysia. Urea and isopropanol (IPA), was provided by QReC Malaysia. Sodium Chlorite (NaClO₂), Sodium Sulphate (Na₂SO₄) (80%), Bisphenol A (BPA), Ammonium Oxalate (AO), and 1,4-benzoquinone (BQ) were procured from Sigma Aldrich. All reagents and chemicals were analytical reagent grade, and no purification step was performed.

2.2. Kapok fibre pre-treatment

Before bio-templated synthesis of g-C₃N₄, the kapok fibres (KF) was undergone NaClO₂ pre-treatment to remove the waxy coating and improved hydrophilicity on its surface according to our previous study [20]. About 1 g of KF was added to 1 wt % of the NaClO₂ solution under magnetic stirring for 10 min. Then, the KF suspension was refluxed at 120 °C for 4 h. Finally, the resultant treated KF was washed with running tap water followed by distilled water and dried overnight in an oven at 65 °C. The NaClO₂ pre-treated KF was named as t-KF.

2.3. Synthesis of bio-templated C-doped porous microtubular g-C₃N₄

The bio-templated C-doped porous microtubular (BTCPM) g-C₃N₄ was prepared using facile direct wet and hydrothermal impregnation followed by thermal condensation. Firstly, 50 g of urea in powder form was dissolved in 75 mL of distilled water. Then, a specific amount of t-KF was added to aqueous urea solution under vigorous stirring for 30 min and followed by sonication for 30 min. For direct wet impregnation, the highly-dispersed t-KF in aqueous urea solution was stored in an oven at 60 °C overnight to evaporate the water, then cooling at room temperature to allow urea recrystallisation. On the other hand, for hydrothermal impregnation, the highly-dispersed t-KF in aqueous urea solution was transfer into 150 mL Teflon-lined stainless-steel autoclave, and the autoclave was sealed and heated at 150 °C for 2 h. Finally, the samples from both impregnation strategy were subjected to the thermal condensation process at 500 °C with the heating rate of 5 °C min⁻¹ for 2 h, using porcelain crucible and lids. The same procedures were repeated by varying the loading of t-KF (wt %) ranging from 0.4 to 2.0 wt %. The resultants samples were denoted as D-0.4, D-0.8, D-1.2, D-1.6, and D-2.0 and h-0.4, h-0.8, h-1.2, h-1.6 and h-2.0 for direct wet impregnation and hydrothermal impregnation, respectively.

2.4. Characterisation

The crystallinity of samples was determined by using Siemens X-ray Diffractometer D5000 with CuKα radiation of wavelength 0.15406 nm at 40 kV and 40 mA. The diffracted intensity was measured by scanning range of 2θ = 5–60° with a step speed of 2°/min. Fourier transform infrared (FTIR) spectra of the samples were obtained using Perkin Elmer infrared spectrometer. Fourier Kratos Analytical Axis Ultra DLD photoelectron spectrometer was used to get the X-ray photoelectron spectroscopy (XPS) spectra of the prepared samples, using Al Kα radiation monochromatic source. The morphological study was carried

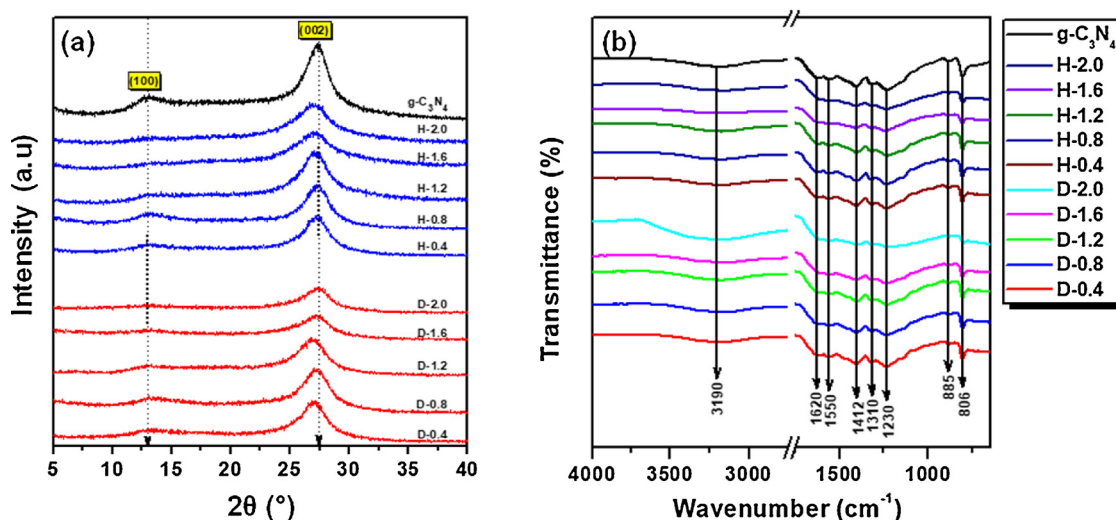


Fig. 1. (a) XRD pattern of bio-templated g-C₃N₄ synthesised with different of t-KF loading (%) by direct wet impregnation (D-0.4, D-0.8, D-1.2, D-1.6, and D-2.0) and hydrothermal approach (H-0.4, H-0.8, H-1.2, H-1.6 and H-2.0). (b) FTIR spectra of prepared BTCPM g-C₃N₄ prepared by both impregnation strategy.

out using field-emission scanning electron microscope (FESEM) (JEOL JSM-7600F, Japan) and transmission electron microscopy (TEM; JEOL JEM-2010HR). Nitrogen adsorption/desorption measurement was performed at -196°C using a Micromeritics instrument (3Flex Version 3.01). Analyses were performed by relative pressure ranging from 0.03 to 0.99. Classic relative pressure range ($P/P_0 = 0.05\text{--}0.20$) was chosen to determine the specific BET surface area. Adsorption/desorption isotherms were used to calculate the pore size distributions with BJH (Barrett-Joyner-Halenda) method. Thermal stability of the sample was characterised using thermogravimetric analyser (Mettler Toledo) from room temperature to 1000°C temperature range under an air atmosphere with the heating rate of $5^{\circ}\text{C min}^{-1}$. The UV–vis Diffuse Reflectance Spectroscopy (DRS) measurements of the prepared samples were assessed using a UV–vis-NIR spectrophotometer (Lambda 950 PerkinElmer). The collected spectra were converted to Kubelka-Munk function, $F(R)$ versus wavelength. The reflection measurements were then converted to absorption spectra using the Kubelka-Munk transformation,

$$F(R) = \frac{(1-R)^{n/2}}{2R} = \frac{K(\lambda)}{S(\lambda)} \propto \alpha = \frac{(h\nu - E_g)^{n/2}}{h\nu} \quad (1)$$

where $F(R)$ is the K–M function or re-emission function, R is the diffuse reflectance of an infinitely thick sample, $K(\lambda)$ is the absorption coefficient, $S(\lambda)$ is the scattering coefficient, $h\nu$ is the photon energy, E_g is the band gap energy, while the value of integer n depends on the characteristics of optical transition ($n = 1$ or 4 for direct or indirect band transition, respectively). It is commonly accepted that the n value for g-C₃N₄ is 4 . The $h\nu$ was derived from $h\nu = hc/\lambda$, where h is Planck constant ($4.136 \times 10^{-15} \text{ eV}$), c is the light velocity in a vacuum ($2.977 \times 10^{17} \text{ nm/s}$), and λ is the wavelength (nm). Photoluminescence spectrum was obtained using Photoluminescence spectrometer (Edinburgh Instrument, FLS920).

2.5. Photoelectrochemical measurement

The photoelectrochemical measurements were performed in a standard three-electrode photoelectrochemical cell connected with a potentiostat (Ametek VersSTAT 4). An Ag/AgCl and a Pt plate were used as the reference and counter electrode, respectively and an aqueous solution containing $0.5 \text{ M Na}_2\text{SO}_4$ (pH 6.2) was used as the electrolyte. The working electrode was prepared by electrophoretic deposition (EPD). 50 mg of prepared samples and 30 mg of iodine were dispersed in acetone and sonicated for 60 min to form a stable colloidal

dispersion. Then, electrophoretic deposition was carried out by immersing two electrodes (Pt foil as an anode, and cleaned FTO as a cathode) were immersed parallel in the solution with a distance between them of 10 mm , and 6 V of bias was then applied between the electrodes for 3 min . The electrodes were then annealed at 200°C for 1 h in the air with a heating rate of 5°C/min to improve its adhesion. The photocurrent was measured under solar AM 1.5 illumination (100 mW cm^{-2}) using a Xenon lamp (ORIEL). The illumination area was set by an aperture to 1 cm^2 . The applied potential was converted into the RHE scale using the Nernst equation; $E_{\text{RHE}} = E_{\text{Ag/AgCl}} + 0.05196\text{pH} + 0.1976$. Electrochemical impedance spectroscopy was carried out in the frequency range of 100 kHz – 100 MHz with AC signal amplitude of 10 mV under open bias condition (i.e. 0.0 V versus Ag/AgCl reference electrode). All photoelectrochemical experiments were performed at room temperature and purged with nitrogen gas for 30 min prior to the electrochemical tests.

2.6. Photocatalytic activity evaluation

10 ppm of Bisphenol A (BPA) used as probe organic pollutants, and a solar AM 1.5 illumination (100 mW cm^{-2}) using a 300-Watt Xenon lamp used as a light source. The photo-degradation reaction temperature was maintained at 25°C by the circulation of water. Before the degradation experiments, the mixed solution of model pollutants (100 mL) and photocatalysts (50 mg) were vigorously stirred for 60 min in the dark to reach the adsorption-desorption equilibrium. Temporal changes in the concentration of BPA were monitored by examining the variation in maximal absorption in the UV–vis spectra at 277 nm .

3. Results and discussion

3.1. XRD analysis

The XRD patterns of all prepared samples were obtained to characterise their crystalline nature and attest their phase purity as shown in Fig. 1(a). The well-developed g-C₃N₄ polymeric network is attained by the presence of two peaks in the XRD patterns. All BTCPM g-C₃N₄ prepared by both impregnation strategy exhibits two characteristic diffractions at 13.1° and 27.5° assigned to the (100) and (002) peaks of graphitic carbon nitride. The peak (100) is attributed to the in-planar repeat period, for example, the hole-to-hole distance among the tri-s-triazine units while (002) is attributed to the typical inter-planar stacking of conjugated aromatic sheets [21–23]. Interestingly, the XRD

signals of the prepared BTCPM by hydrothermal impregnation exhibits more intense and sharp peak which indicated higher crystallinity than those made by direct wet-impregnation. However, increased in t-KF loading up to 1.6 and 2.0 wt % for both impregnation strategy, revealed the lower and broader in peak intensity of (100) and (002) planes in which more prominent for samples obtained by direct wet-impregnation. These phenomena suggest that BTCPM g-C₃N₄ sample has less degree of condensation and smaller domain size [24]. It can be due to the extensive C dopant in the BTCPM g-C₃N₄ structure which effectively inhibits the growth of crystallites and hinders phase transformation. Similar observation also can be found elsewhere with different dopant species (e.g. Na, O, B, P) [25–28]. Moreover, it was postulated that this observation might be due to polymer-like growth was dominated in BTCPM g-C₃N₄ by direct wet impregnation compared to the growth of a graphitic structure in BTCPM g-C₃N₄ by hydrothermal [3]. Compared with pristine g-C₃N₄, the peak at 27.5° of BTCPM g-C₃N₄ was slightly shifted toward lower 2θ value as the C doping in BTCPM g-C₃N₄ caused crystal lattice distortion [7]. From the XRD analysis, the BTCPM g-C₃N₄ prepared by hydrothermal impregnation strategy could promote the formation of compact structure and high crystalline BTCPM g-C₃N₄ as compared to direct wet impregnation.

The formation of g-C₃N₄ using bio-templates approach can be further proven by Fourier transform infrared (FTIR) spectroscopy analysis as shown in Fig. 1(b). The obtained BTCPM g-C₃N₄ spectra showed similar absorption region with previous studies [28,29]. In the FT-IR spectra of all samples, the broad peak at 3190 cm⁻¹ can be attributed to stretching mode of the N–H bond and the peaks located at about 1240, 1320, 1400, 1430, 1570 and 1640 cm⁻¹ are ascribed to aromatic C–N stretching vibration modes and C=N stretching vibration modes [26,29]. The peak at 806 cm⁻¹ is originated from characteristic breathing vibration of tri-s-triazine units ring [30]. From the FTIR analysis, there are no significant differences in peak assignment position of the BTCPMs g-C₃N₄ prepared by both impregnation strategy except its peak assignment intensity. In comparison with pristine g-C₃N₄, the BTCPM g-C₃N₄ prepared by both impregnation strategy shows slightly reduced the intensity of primary peak assignment. It can be explained by the presence of C dopant in g-C₃N₄ distort in its original functional group vibration (C–N stretching vibration modes and C=N stretching vibration modes).

3.2. Chemical composition analysis

The direct evidence on doping of carbon was further confirmed through XPS analysis. The survey spectra of prepared samples were depicted in Fig. 2. From the survey spectra, it shows two dominant peaks represent the elements of C and N and a weak signal of a trace of O elements in the prepared sample. The surface compositional analysis of all prepared samples obtained from XPS analysis was tabulated in Table S1. The C 1s high-resolution spectra of pristine g-C₃N₄ can be deconvoluted into two main peaks at 284.8 eV and 288.3 eV. The peak at 284.8 eV can be assigned to the C–C adventitious carbon species. However, the fitted C 1s high-resolution spectra of BTCPMs g-C₃N₄ samples were fitted into three main peaks at 284.8, ~286.3–286.6, and 288.3 eV. The highest and intense peak at 288.3 eV for C 1s peak, corresponding to sp³ N=C–N₂ coordination, is ascribed to carbon atoms that have one double and two single bonds with three N neighbours [7,31–33]. The peak at the valley (286.3–286.6 eV) was corresponded to the sp² C–N–C [34] or C–NH₂ species [35]. The broad region at- 292–294.3 eV was attributed to π-π* excitations between the graphitic layers [3]. However, there is another one peak was observed at- 290 eV for BTCPM g-C₃N₄ samples prepared by hydrothermal impregnation which can be ascribed to C–O. The presence of oxidised carbon could be caused by a slightly oxidation during the synthesis of graphitic carbon nitride which is carried out under air [24].

In addition, the BTCPM g-C₃N₄ samples prepared from both impregnation strategies exhibit quite similar N 1s which fitted at around-

398.8, 400.0, 401.0, and 403–404 eV. These peaks can be attributed to sp²-hybridized nitrogen (C–N–C) [7], sp³-hybridized nitrogen (N–[C]₃) [28,29], amino functional groups with a hydrogen atom (C–N–H) [26], and π-π* excitations [3,6] respectively. The fitted peaks for high resolution of C 1s and N 1s spectra for all samples were summarized in Table S2. Combined with high-resolution C 1s, it is trustworthy to note that, the intensity for sp² C–N–C peak was increased significantly with the increment of t-KF loading. Furthermore, the C/N ratio estimated from the XPS analysis (Table S1) indicated an increase from 0.75 (theoretical value) for bulk g-C₃N₄ to more than 1.00 for BTCPM g-C₃N₄ samples. In addition, the C/N ratio value could be increased with the increasing of t-KF during the preparation of BTCPM g-C₃N₄. All these data demonstrate that some sp²-hybridized nitrogen atoms in the BTCPM g-C₃N₄ could be substituted by C atoms by in situ carbon doping in bio-templates synthesis route using t-KF. Again, the obtained BTCPM g-C₃N₄ by hydrothermal impregnation significantly increased the C doping in sp² C–N–C. It is already reported that the replacement of bridging nitrogen by carbon due to doping, could create large delocalized π bonds that enhances the electrical conductivity and impedes the electron hole recombination. The presence of large delocalized π bonds is also reported to favor increased adsorption of organic moieties due to strong π–π interactions which can be led to the higher photo-degradation activity [35].

We also observed an O 1s XPS peak at around 532.5 eV for both group of BTCPMs g-C₃N₄ samples (Fig. S1). Combining with the peak at 286.26 eV in the C1s spectra, we retrieved the XPS database of C1s and O1s and determined it to be C–O, which could be from the adsorbed CO₂ and isocyanic acid (HN=C–O), or incompletely reacted oxygen-containing intermediates produced during the pyrolysis of urea [24,36]. Also, the peak at- 533.5 eV can be assigned to the chemisorbed H₂O.

3.3. Morphological, structural and textural analysis

Naturally, the raw kapok fibre possessed high hydrophobic properties. Therefore, before the synthesis step, the raw kapok fibre was undergone chemical pre-treatment to remove of surface wax from the kapok fibre and subsequent exposure of hydrophilic hydroxyl groups [20]. The raw KF exhibited microtubular structure with rough and thicker outer surface [Fig. 3(a)], while the treated kapok fibre (t-KF) shows the smoother and thinner outer surface [Fig. 3(b)]. This observation indicated excellent removal of surface wax and improve hydrophilicity properties using NaClO₂ pre-treatment method. The improve hydrophilicity properties were observed when the t-KF could be immersed in the water while the raw KF floated on the water surface. The pre-treatment would lead to the enhancement of urea impregnation on the surface of t-KF in aqueous solution and well-developed g-C₃N₄ mimicking the original structure of KF could be expected.

The FESEM images of the resultant BTCPM g-C₃N₄ samples obtained by Fig. 3(c–e) direct wet impregnation and Fig. 3(f–h) hydrothermal impregnation strategy. The major differences between these both impregnation are that the morphology of BTCPM g-C₃N₄ samples obtained by hydrothermal impregnation shows the more well-constructed microtubular structure and even g-C₃N₄ wrapping than shows in BTCPM g-C₃N₄ samples obtained by direct wet impregnation. The high magnification FESEM images of both BTCPM g-C₃N₄ exhibited the uniform 2D flake structure and unfolded at the edge of the g-C₃N₄ sheet. The TEM and HRTEM images of sample H-0.8 shown in Fig. 3(i) and (j). The HRTEM shows the resultants BTCPM g-C₃N₄ possess porous structure. The microtubular and porous structure is beneficial for light absorption and scattering improved adsorption of organic pollutants in aqueous solution and induced excellent charge separation. The presence of porous structure resulted from cyanuric decomposition. Our previous study revealed that the cyanuric acid is less thermally stable than melamine, and it decomposed into gases at an elevated temperature, which responsible for the creation of the porous structure of BTCPM g-

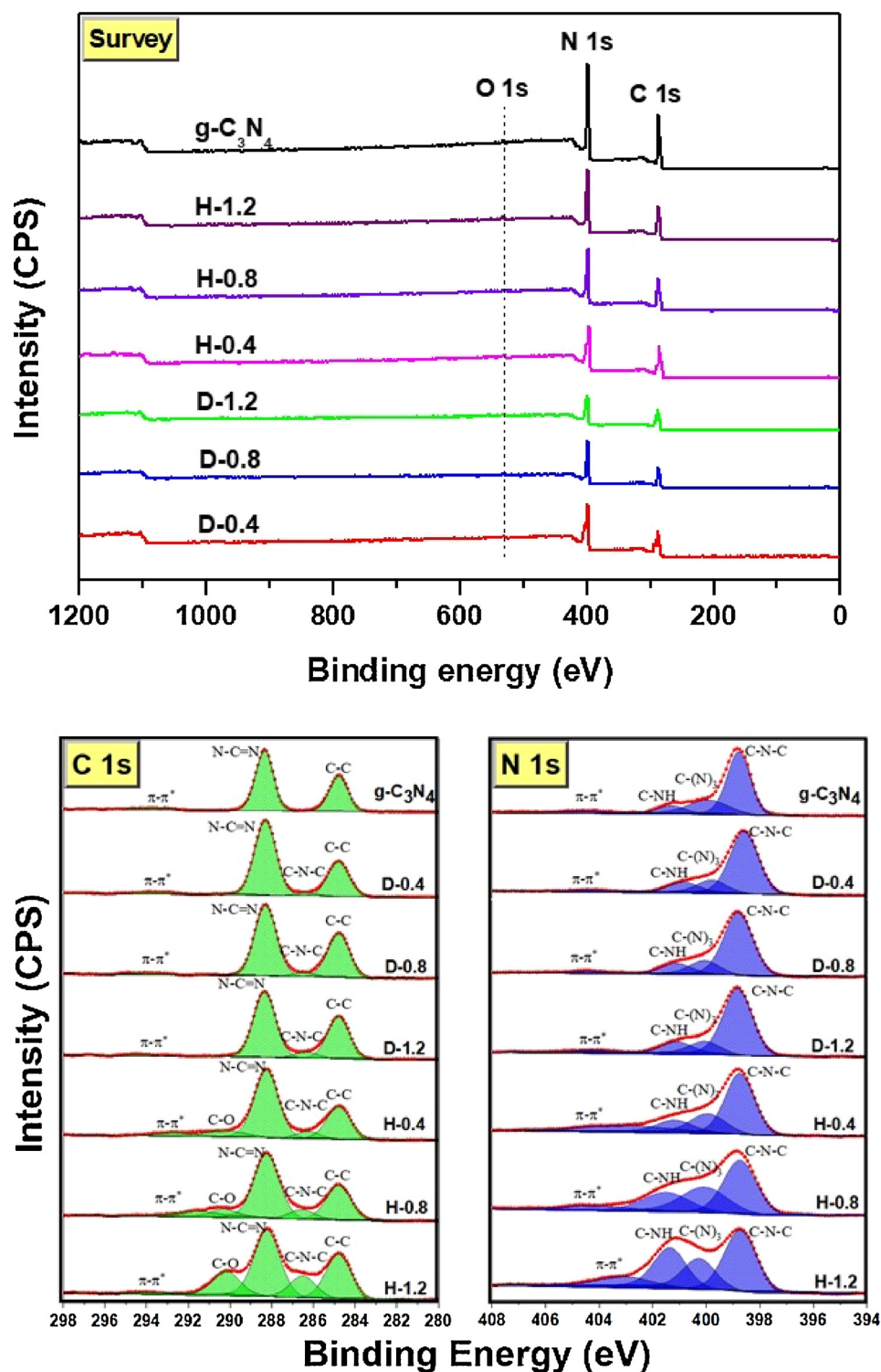


Fig. 2. XPS survey and high-resolution spectra of C1s and N1s of BTCPM g-C₃N₄ synthesised with different of t-KF loading (wt %) by direct wet impregnation (D-0.4 – D-1.2) and hydrothermal approach (H-0.4 – H-1.2).

C₃N₄ [Fig. 3(j)] with an increased surface area and would lead to the efficient charge separation [21].

The fitting adsorption plot corresponding to the bio-templated g-C₃N₄ prepared with different t-KF loading is displayed in Fig. 4. The BET surface area, total pore volume and average pore size values are tabulated in Table S3. The curves showed that overall N₂ sorption isotherms are typical for type IV with a steep H₃ hysteresis loop in the relative pressure of (P/P₀) range of 0.80–1.00, further validate the

existence of mesoporous features (2–50 nm) and three-dimensional (3D) intersection of porous materials. The textural characteristics of pristine g-C₃N₄ were obtained with a specific surface area of 48.6 m²g^{−1} with a pore size of 42.8 nm (Fig. 4a). As compared to pristine g-C₃N₄, the bio-templated g-C₃N₄ possessed a low BET surface area, particularly for D-0.4 and H-0.4. It was commonly accepted that the lower in BET surface area is corresponding to the larger particles size. In this study, the utilisation of kapok fibre as via bio-templated would

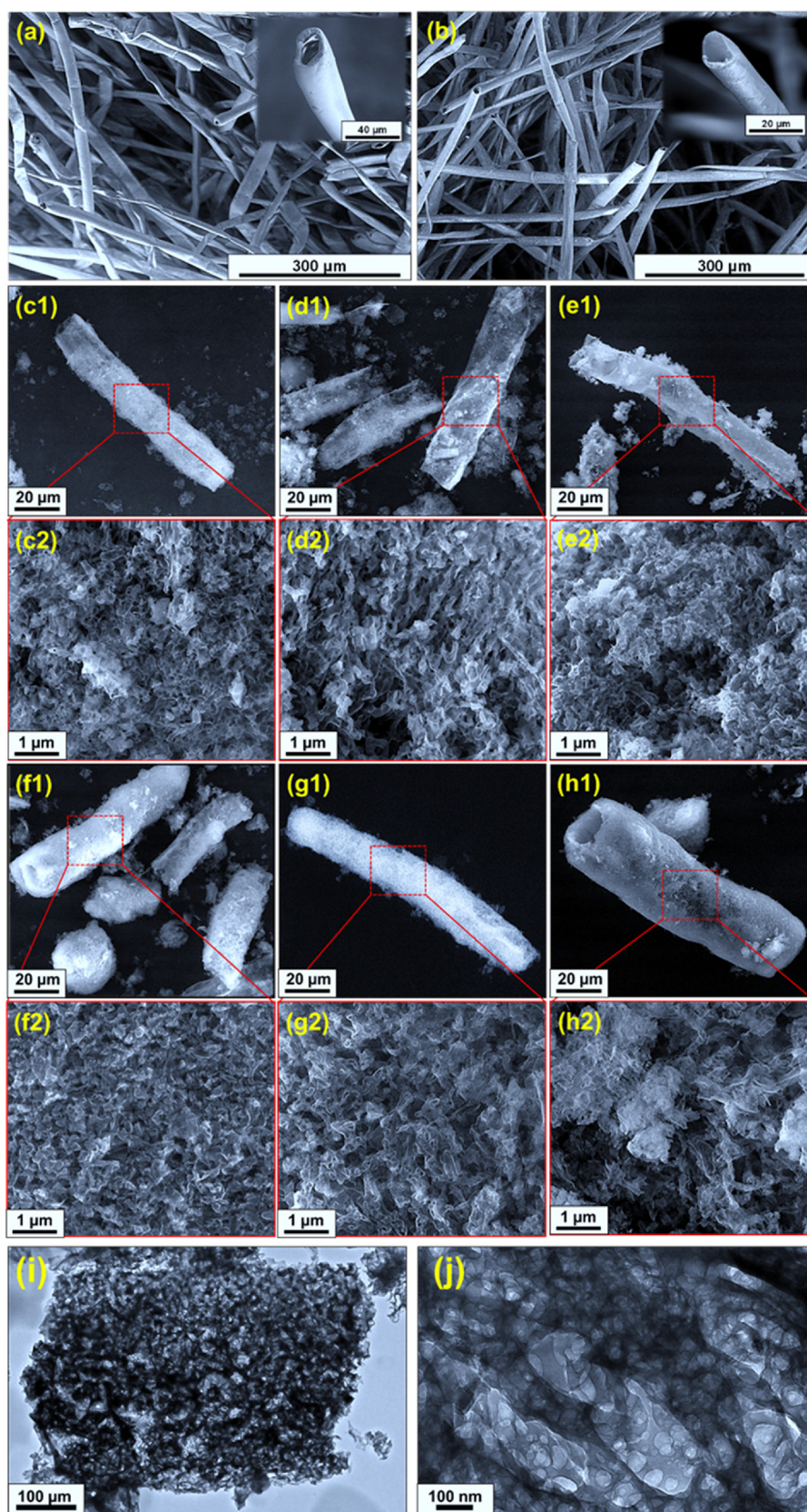


Fig. 3. FESEM images of (a) raw KF, (b) t-KF, BTCPM g-C₃N₄ synthesised by (c–e) direct wet impregnation [(c) D-0.4, (d) D-0.8, and (e) D-1.2] and (f–h) hydrothermal approach [(f) h-0.4, (g) h-0.8, and (h) h-1.2]. (i & j) TEM and HRTEM images of sample H-0.8.

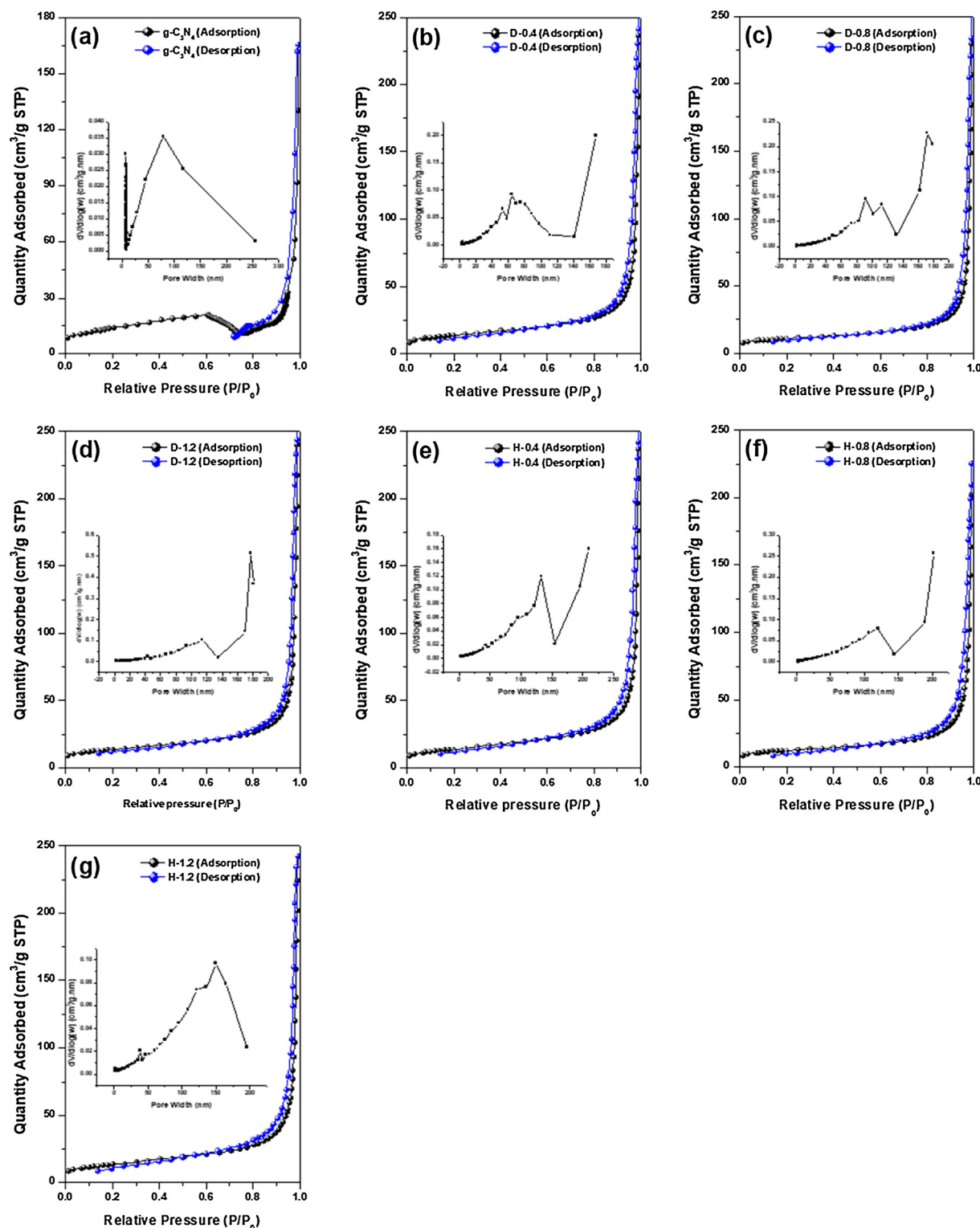


Fig. 4. N_2 adsorption-desorption isotherms and BJH pore size distribution (inset) of prepared bio-templated $g-C_3N_4$ direct wet impregnation and hydrothermal approach with different t-KF loading.

result in microtubular $g-C_3N_4$ which are larger than the pristine $g-C_3N_4$ which consist of nanosheet structure which responsible for the higher surface area. It was found that the capillary condensation predominates in the samples from hydrothermal synthesis has larger surface area and pore size than direct impregnation method when increasing the t-KF loading up to 0.8 wt% ($49.6 \text{ m}^2 \text{ g}^{-1}$, 27.8 nm) for sample H-0.8. It was found to reduce upon addition of a higher amount of t-KF at 1.2 wt%

($47.7 \text{ m}^2 \text{ g}^{-1}$, 26.7 nm) for sample H-1.2. It is trustworthy to note that the higher amount of t-KF could promote better interaction of urea-precursor with the polar hydroxyl groups of t-KF to form the larger size of microtubular $g-C_3N_4$. Nevertheless, the pore volume of the sample prepared via direct impregnation showed an increment in comparison to pristine $g-C_3N_4$, but there is no significant difference in the values among the samples obtained. While, samples prepared from

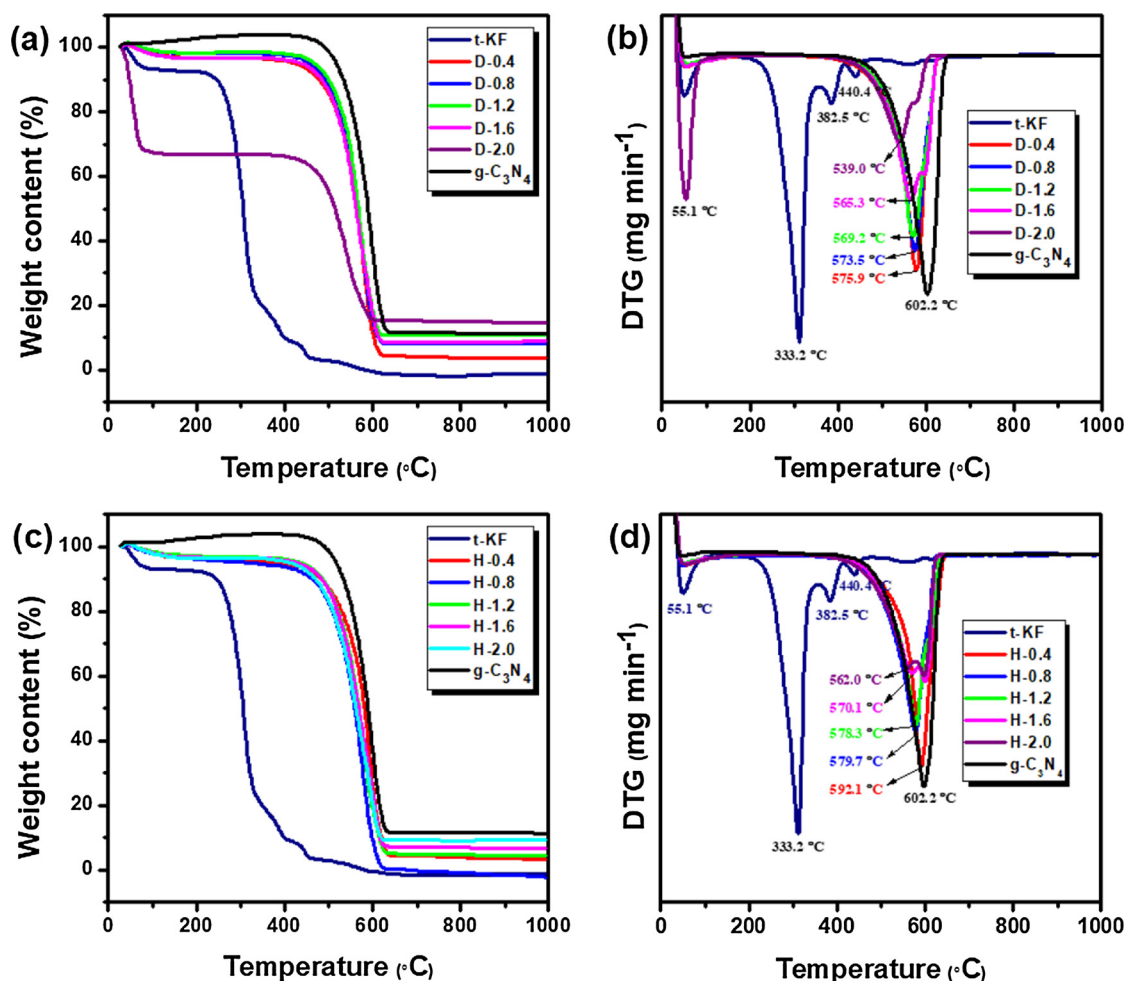


Fig. 5. TGA and DTG curves of prepared BTCPM $g-C_3N_4$ (a & b) direct wet impregnation and (c & d) hydrothermal approach with different t-KF loading.

hydrothermal displayed some pore volume reduction when increasing the amount of t-KF, suggesting the presence of disordered pore shapes as characteristics of the samples. The corresponding pore size distributions from BJH method (inset) also displayed quite broad for pristine $g-C_3N_4$ and H-1.2 samples which implies the deterioration of the porous structures of the two samples and the presence of large mesopores and small macropores in the lattice [37]. The hierarchical structures of the other samples with mesopores are also expected to provide more active sites which render faster migration of charge carriers by inhibiting the recombination of electron-hole, resulting in a higher photoreaction quantum efficacy [38].

3.4. Thermogravimetric analysis

The thermogravimetric analysis was conducted to elucidate the formation and effect of t-KF loading on the resultants BTCPMs $g-C_3N_4$ prepared from both impregnation strategy. The thermal stability profile of t-KF exhibited four stages of degradation as can be seen in Fig. 5. The initial weight loss at 55.1 °C was due to the evaporation of moisture content on the surface of the samples [20]. The drastic weight loss was observed at 333.2 °C was due to decomposition of cellulose while weight loss at 382.5 and 440.4 °C was attributed to the decomposition of hemicellulose and lignin [39]. Thus, the complete removal of the t-KF template is expected during the preparation of the BTMC $g-C_3N_4$ at a calcination temperature of 500 °C. The BTCPMs $g-C_3N_4$ prepared from both impregnation strategy exhibited similar decomposition mechanism as can be observed in Fig. 5(a–d). Our previous study indicated that the transformation of $g-C_3N_4$ from urea as starting material

involved four stages of phase transformation which are (i) urea > cyanuric acid at 229.1 °C, (ii) cyanuric acid > melamine at 348.6 °C, (iii) melamine > melem at 377.7 °C, and (iv) melem > $g-C_3N_4$ at 408.3 °C [21]. Thus, in this study, the well-constructed of BTCPMs $g-C_3N_4$ is accomplished at a calcination temperature of 500 °C which accordance with our XRD, FTIR, FESEM, TEM and XPS analysis. The plausible BTCPMs $g-C_3N_4$ formation through direct wet impregnation and hydrothermal approach is schematically presented in Fig. 6.

The complete decomposition of pristine $g-C_3N_4$ could be attained at a temperature of 602.2 °C (Fig. 5). However, as compared to pristine $g-C_3N_4$, the complete decomposition of BTCPMs $g-C_3N_4$ could be attained at a lower temperature between 539.0 °C to 575.9 °C and 562.0 °C to 592.1 °C for BTCPMs $g-C_3N_4$ prepared by direct wet impregnation and a hydrothermal method, respectively. This observation indicated that the thermal stability of the prepared BTCPMs $g-C_3N_4$ reduced significantly. Moreover, as can be seen in Fig. 5(b) and (d), the thermal stability of the prepared BTCPMs $g-C_3N_4$ is also reduced with the increased in t-KF. The in-situ carbon doping in BTCPMs $g-C_3N_4$ can explain the phenomena which initially came from t-KF which has explained in section 3.2, where the higher t-KF loading would result in higher in-situ carbon doping. It is commonly accepted that the chemical characteristic of the tri-s-triazine ring is responsible for the higher thermal stability of pristine $g-C_3N_4$ up to 600 °C [40,41]. Therefore, the in-situ carbon doping by carbon substitution with the sp^2 -hybridized nitrogen atoms in the BTCPMs $g-C_3N_4$ suggestively disturb the original chemical characteristic of the tri-s-triazine ring and results in a reduction of the overall thermal stability. Interestingly, the BTCPMs $g-C_3N_4$ prepared by hydrothermal impregnation strategy exhibited better thermal stability

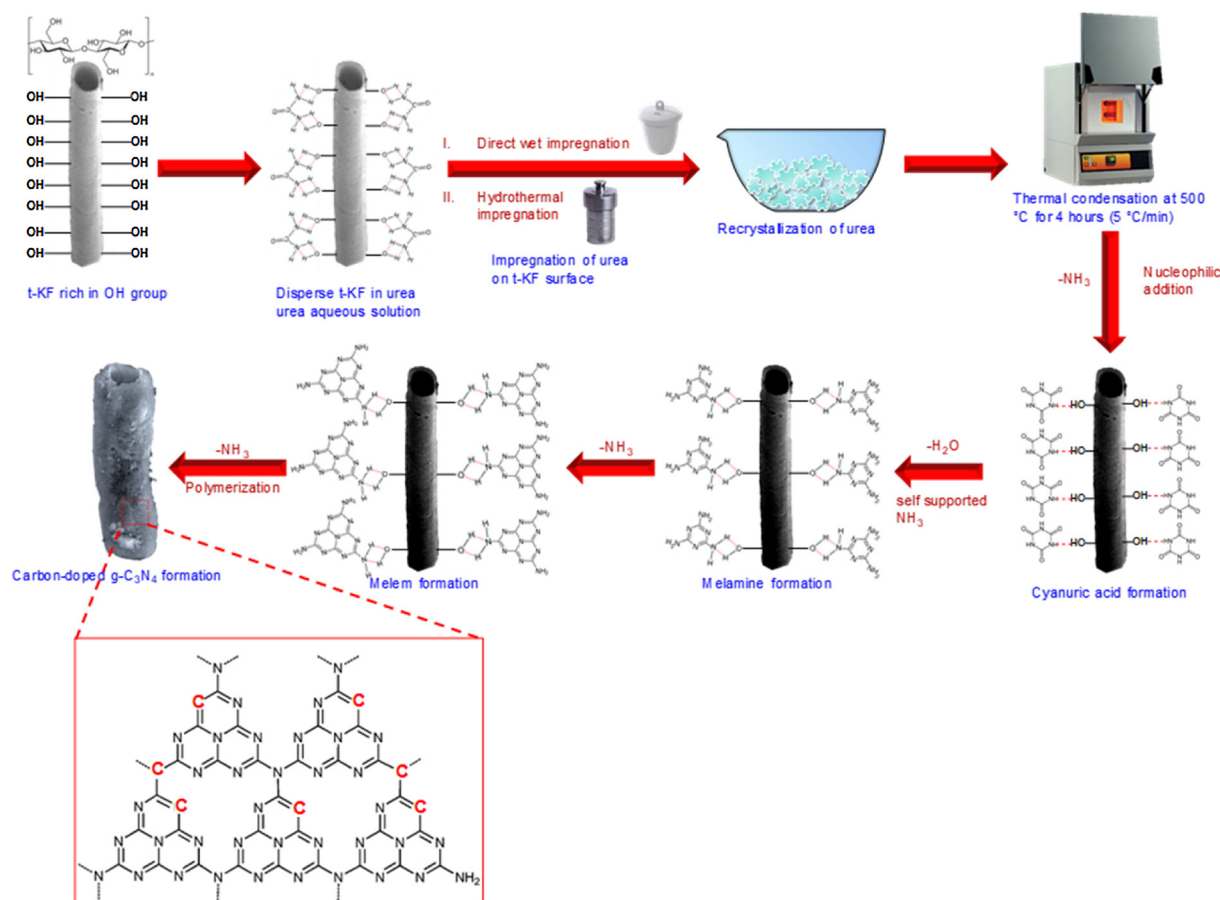


Fig. 6. Plausible BTCPM $g\text{-C}_3\text{N}_4$ formation mechanism through direct wet impregnation and hydrothermal approach.

as compared to the BTCPMs $g\text{-C}_3\text{N}_4$ prepared by direct wet impregnation strategy. It can be explained by the compact structure and relatively higher in crystallinity of the BTCPMs $g\text{-C}_3\text{N}_4$ prepared by hydrothermal impregnation strategy which good agreement with XRD and FESEM analysis. The summary of thermal stability data of prepared BTCPMs $g\text{-C}_3\text{N}_4$ direct wet impregnation and hydrothermal approach with different t-KF loading is tabulated in Table S4.

3.5. Optical properties

The diffuse reflectance spectra, Kubelka-Munk curves and band gap determination of each sample were shown in Fig. 7(a & d), (b & e), and (c & f), respectively. As can be seen in the Kubelka-Munk curves [Fig. 7(b) & (e)], all BTCPM $g\text{-C}_3\text{N}_4$ samples obtained from both impregnation strategy possessed excellent optical absorption capability up to the near-infrared (NIR) region as compared to pristine $g\text{-C}_3\text{N}_4$. The absorption of photon energy up to the NIR region become prominent with the loading of t-KF up to 1.0. Undeniably, the t-KF loading gives significantly influenced to their optical absorption capability which provides more carbon doping the BTCPM $g\text{-C}_3\text{N}_4$ structure. The excellent light absorption of BTCPM $g\text{-C}_3\text{N}_4$ over the entire wavelength range, which is primarily due to the microtubular and mesoporous structure which induced the multiple reflections of incident light within the structure. It can be postulated that when the incident light irradiates the scattering surface, the light will be scattered throughout the mesoporous microtubular structure. The scattered light has a longer optical path and thus is more readily absorbed. The ability to absorb photon energy up to NIR region would be more practical for the material in full utilisation of solar irradiance and can lead to improvement in their photocatalytic activity.

In order to better classify the prepared BTCPM $g\text{-C}_3\text{N}_4$ as a

potentially potent photocatalyst for specific applications, i.e., photo-degradation of organic dyes/pollutant, photocatalytic water splitting, photocatalytic carbon dioxide reduction and so on; a knowledge of their band energy levels is essential. Thus, the effect of t-KF loading on the band gap structure was further elucidated by obtaining their band gap edges position. The CB and VB edge positions of the as-prepared samples can be calculated according to the Mulliken electronegativity theory. Herein, the electronegativity of an atom is the arithmetic mean of the atomic electron affinity and the first ionisation energy [42]. The valence band (VB) and conduction band (CB) positions were determined by using the following reactions [43–45];

$$E_{VB} = X - E_e + 0.5E_g \quad (2)$$

$$E_{CB} = E_{VB} - E_g \quad (3)$$

where E_{CB} and E_{VB} are the bottom conduction bands (CB) and the top of the valence band (VB) relative to the normal hydrogen electrode (NHE) and E_g means the band gap energy of the photocatalyst, E_e is the energy of free electrons (4.5 eV), X is the electronegativity of the semiconductor (X value for $g\text{-C}_3\text{N}_4$ is 4.73), which is the geometric mean of the electronegativity of the constituent atoms [22,46]. Table 1 presenting the calculated band gap of the resultants samples.

To realise the practicability of the photocatalyst in the broad solar spectrum, the bandgap should not be too wide to allow the absorption of photons from the visible and NIR part of solar radiation. The band gap structure of BTCPMs $g\text{-C}_3\text{N}_4$ samples obtained from both impregnation strategy with the t-KF loading between 0.4 to 1.2 are acceptable to be utilised as a photocatalyst for water splitting hydrogen production and CO_2 photoreduction (Fig. 8). Furthermore, the resultants photocatalyst are expected to be unable to direct formation of hydroxyl radical which responsible for photodegradation of hazardous organic

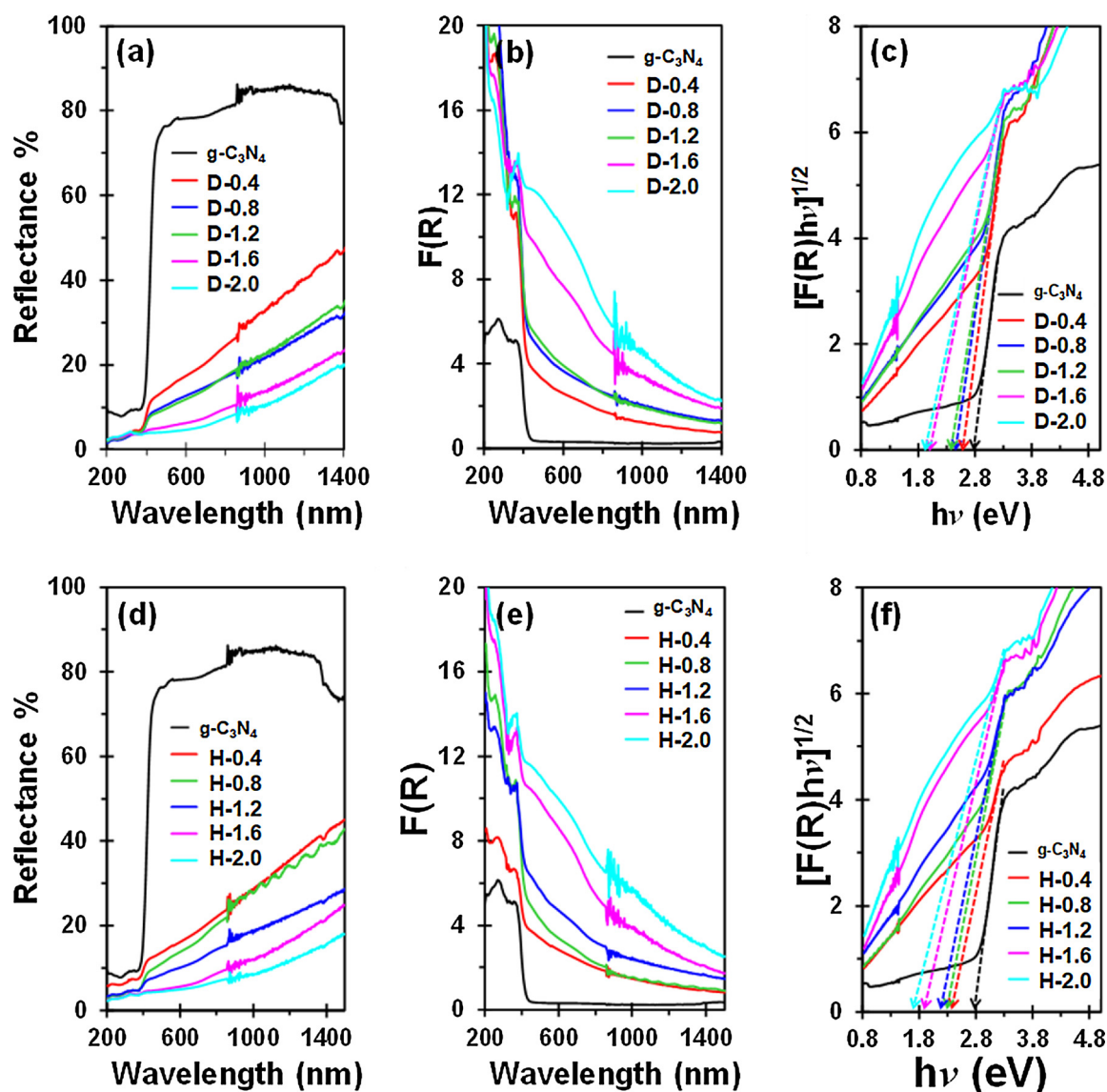


Fig. 7. (a,d) Diffuse reflectance (%R) spectra, (b,e) Kubelka-Munk curves, and (c,f) band gap determination by drawing the line at $[F(R)h\nu]^{1/2} = 0$ of BTCPMs $g-C_3N_4$ synthesised with different of t-KF loading (%).

Table 1
Estimated band gap, valence and conduction band edges.

Sample	Band gap (eV)	E_{VB} (eV)	E_{CB} (eV)
$g-C_3N_4$	2.75	1.61	−1.14
D-0.4	2.58	1.52	−1.06
D-0.8	2.45	1.46	−0.99
D-1.2	2.38	1.42	−0.96
D-1.6	2.00	1.23	−0.77
D-2.0	1.90	1.18	−0.72
H-0.4	2.35	1.41	−0.94
H-0.8	2.28	1.37	−0.91
H-1.2	2.15	1.31	−0.84
H-1.6	1.88	1.17	−0.71
H-2.0	1.68	1.07	−0.61

pollutants in aqueous solution. It is because the valence band of the BTCPMs $g-C_3N_4$ does not straddle the redox potential of hydroxyl radicals. In the meantime, the obtained bandgap structures for the sample (D-0.4, D-0.8, D-1.2, H-0.4, H-0.8, and H-1.2) straddled the redox potentials for water photolysis and CO₂ reduction. However, based on BTCPMs $g-C_3N_4$ samples band gap alignment, the organic pollutants

could be degraded by superoxide radical ($\cdot O_2^-$) since their conduction band position is more negative than $O_2/\cdot O_2^-$ reduction potential. The capability of BTCPM $g-C_3N_4$ sample in degrading the hazardous organic pollutants was further elucidated in photocatalytic activity section.

3.6. Charge carrier separation behaviour

In order to efficiently utilised for photocatalysis application, the charge carrier separation of the obtained samples of D-0.4, D-0.8, D-1.2, H-0.4, H-0.8, and H-1.2 were elucidated. The excellent charge carrier behaviour becomes necessary attributes to ensure a better photocatalytic performance. Principally, the higher photocatalytic activity upon light irradiation can be associated with the excellent electron-hole pairs separation and charge transfer. In this study, understanding on the effectiveness of electron-hole pairs separation and charge transfer of all prepared photocatalysts were elucidated by photocurrents response, Applied bias photon-to-current efficiency (ABPE), electrochemical impedance spectroscopy (EIS), and photoluminescence (PL). The photocurrent response versus the applied potential of all prepared samples, using the linear sweep voltammetry mode in potentiostat, is shown in

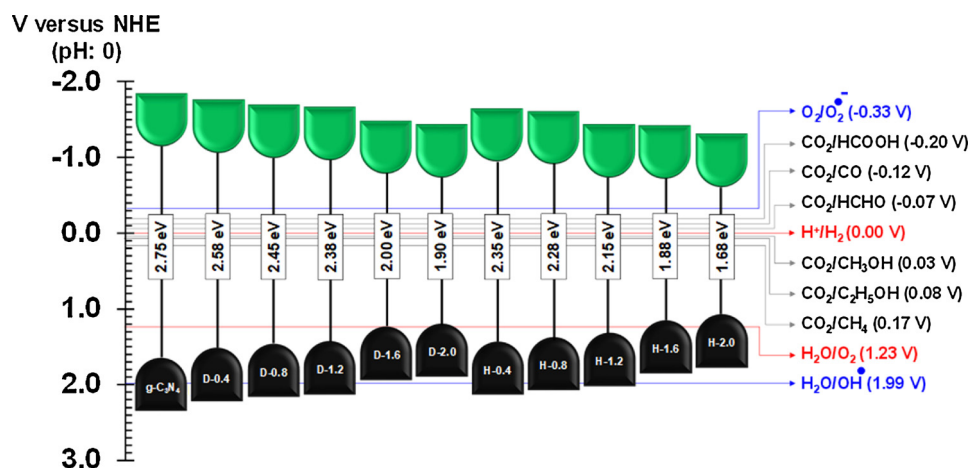


Fig. 8. Band gap alignment of synthesised BTCPM g-C₃N₄ samples.

Fig. 9(a). Based on the photocurrent density plot, all prepared samples depicted the positive curves, suggesting all prepared samples are n-type semiconductors with electrons as the majority carriers. BTCPMS g-C₃N₄ samples with 0.8 wt % t-KF loading exhibited the highest photocurrent density [Fig. 9(a)]. The ABPE% with the BTCPMS g-C₃N₄ obtained by hydrothermal impregnation show remarkably photocurrent response [Fig. 9(b)]. The highest photocurrent density and ABPE% indicated excellent photoinduced electron-hole pairs. Electrochemical impedance spectroscopy (EIS) is an intuitional approach to gain more profound insights into the charge transport behaviour. The EIS Nyquist Plot of all

prepared samples is shown in Fig. 9(c). The arc radius of the semi-circular Nyquist Plot of BTCPMS g-C₃N₄ samples with 0.8 wt % t-KF loading obtained by hydrothermal impregnation (H-0.8) was the smallest when compared to pristine g-C₃N₄ and other samples. It was suggested that this sample has the lowest electron-transfer resistance and highest electrical conductivity. The smaller the arc radius of an EIS Nyquist Plot means the higher the efficiency of charge separation.

In order to verify the findings, we conducted the photoluminescence (PL) spectroscopy to study the trapping, migration and electron-hole pair recombination of the semiconductor. The semiconductor would

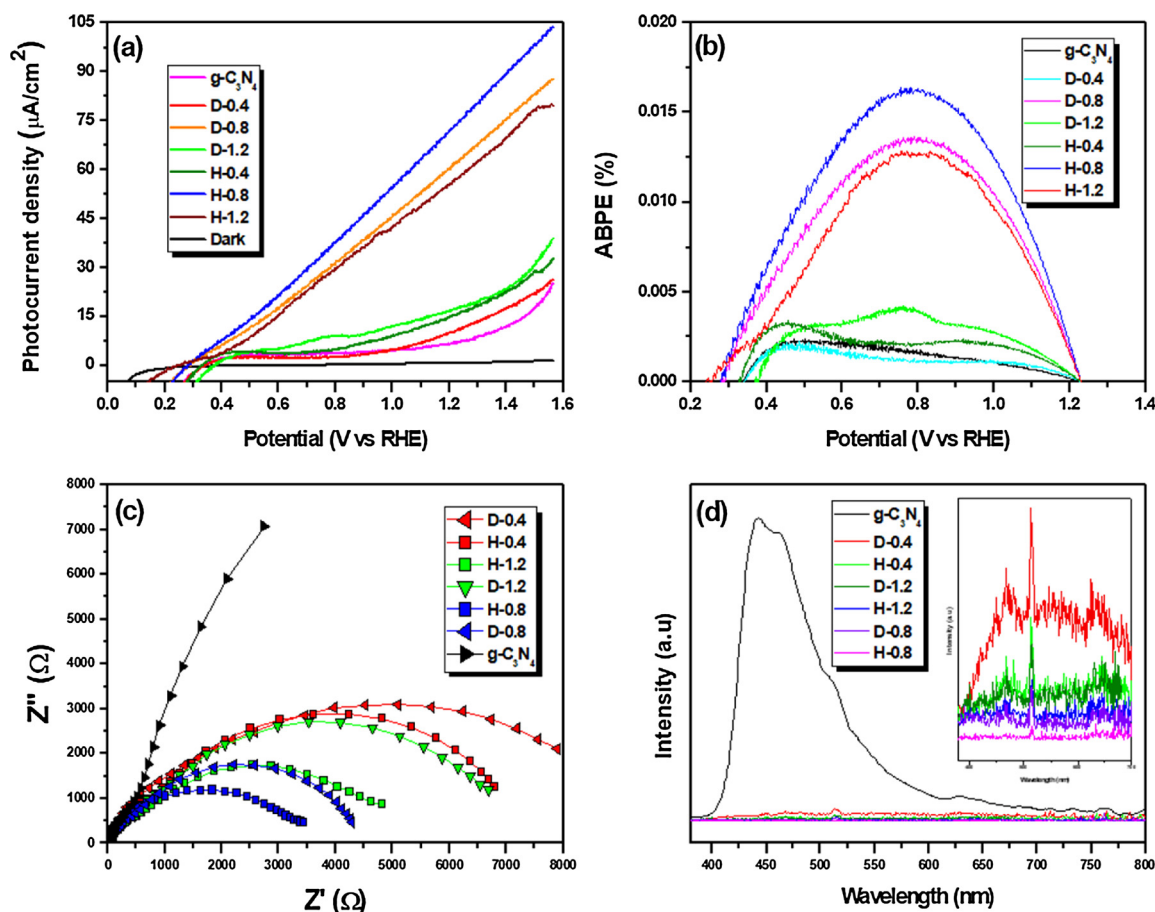


Fig. 9. (a) Photocurrent density versus applied potential (V vs RHE), (b) Applied bias photon-to-current efficiency (ABPE), (c) Nyquist plot of electrochemical impedance spectra under visible irradiation, and (d) Photoluminescence spectra of prepared bio-templated g-C₃N₄ direct wet impregnation and hydrothermal approach with different t-KF loading (0.4, 0.8, and 1.2 wt%).

emit photons that resulted in photoluminescence due to the electron-hole pair recombination after the semiconductor was irradiated. Fig. 9(d) shows the PL spectra of all BTCPMS g-C₃N₄ samples. The pristine g-C₃N₄ exhibited the highest distinct emission band at 438 nm which can be explained due to the electron-hole pair being attracted to each other in its bound state. Thus, the higher peak intensity was attributed to the rapid recombination of the electron-hole pair, lead to the reduction of the photocatalytic activity performance. Furthermore, the previous study suggested that the hierarchical tubes structures promote the redistribution of electrons in one side and holes in the other side driven by the band offsets [29,47] and consequently, the inherent drawback of fast electron-hole recombination in pristine g-C₃N₄ can be resolved. Thus, a better photocatalytic performance of BTCPMS g-C₃N₄ samples can be expected. The microtubular with open-end also facilitates the charge carrier transfer migrating to photocatalyst surface, thus leading to low radiative PL emission [29]. Significantly, the incorporation of in-situ carbon doping in BTCPMS g-C₃N₄ would lead to the enhancement of the conductivity and electron redistribution for the excellent charge carrier separation.

3.7. Photocatalytic activity

The photocatalytic properties of the resultants BTCPMS g-C₃N₄ were evaluated by photodegradation of bisphenol A (BPA) under visible light irradiation. As shown in Fig. 10(a), the photolysis of BPA in the absence of photocatalysts indicated that it is very stable and resistant to photodegradation under visible light irradiation. On the other hand, photodegradation of BPA using pure TiO₂ (P25) is considerably low as this photocatalyst well known as UV light active photocatalyst due to its

large band gap (3.2 eV). Even though the pristine g-C₃N₄ possessed smaller band gap than TiO₂ (P25) which is 2.75 eV, its capability in degrading the BPA under visible light irradiation is low with the percentage of photodegradation of 24%. The low photocatalytic activity of pristine g-C₃N₄ was contributed to its rapid electron-holes recombination rate as revealed in Section 3.6. The previous study postulated that the pristine g-C₃N₄ displayed insufficient charge separation and poor charge mobility, both of which lead to low photocatalytic activity [32,48].

Interestingly, the prepared BTCPMS g-C₃N₄ significantly improved the photocatalytic activity where the BTCPMS g-C₃N₄ prepared by hydrothermal impregnation approach revealed the highest percentage degradation of BPA as compared to direct impregnation approach. Moreover, the variation of t-KF loading during the synthesis of BTCPMS g-C₃N₄ via both impregnation strategy could significantly affect its photocatalytic activity. It was found that the addition of 0.8 wt % t-KF possessed the highest photocatalytic activity with percentage degradation of BPA were 91.0% and 80.2% for sample H-0.8 and D-0.8, respectively. However, as the loading of t-KF was added up to 1.2 wt %, the overall photocatalytic of the prepared BTCPMS g-C₃N₄ (D-1.2 and H-1.2) was suppressed significantly. As discussed in XPS analysis, the increased in t-KF wt % resulted increased in carbon doping concentration in BTCPMS g-C₃N₄. Therefore, the band gap of the prepared BTCPMS g-C₃N₄ became much narrower which increasing t-KF wt %. Thus, the much narrow of the space charge region between valence and conduction band could be expected. Consequently, under this circumstance, the recombination of the electron-hole pairs would become easier and resulting decrement of the photocatalytic activities of the photocatalyst. Therefore, the appropriate and optimal band gap value

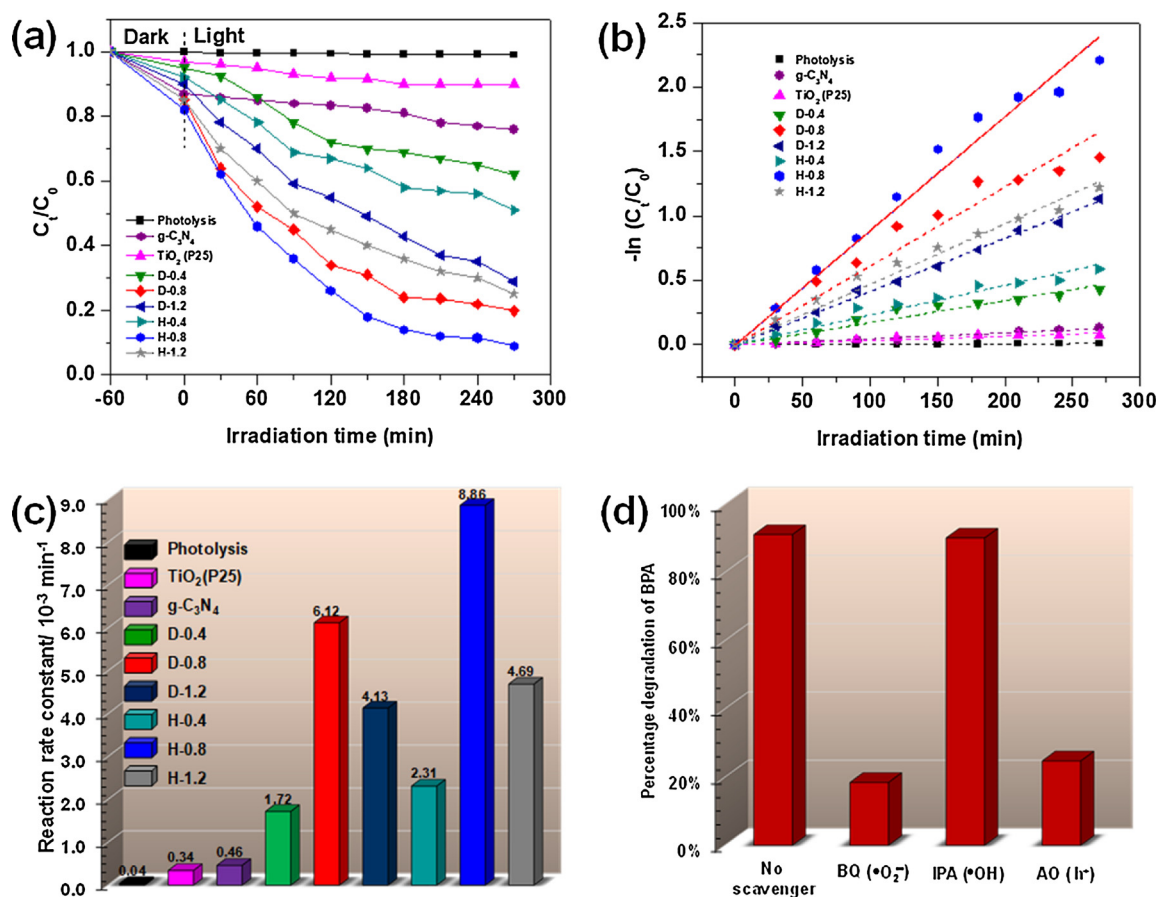


Fig. 10. (a) Photodegradation rate of BPA under visible light irradiation for 270 min on all samples. (b) Kinetics of the disappearance of BPA degradation of all samples. (c) The reaction rate constant of all samples. (d) Effect of various scavengers on the visible-light photocatalytic activity of BTCPMS g-C₃N₄ (H-0.8) towards the degradation of BPA.

and carbon doping contents should be vitally determined to prepare high efficient photocatalyst.

In principle, the photocatalytic reaction presumably occurred on the surface of the catalyst surface for a heterogeneous photocatalytic system. Therefore, high adsorption capability would lead to the more elevated photocatalytic activity. As shown in Fig. 10(a), all sample indicated reasonable adsorption capability in dark condition due to the presence of sizeable delocalized π bonds which promotes adsorption of BPA due to strong $\pi-\pi$ interactions [35]. Moreover, the sample H-0.8 exhibited the highest adsorption capability because it possessed the highest surface area as compared to other samples. Consequently, the high in surface area would provide a more active surface area for physisorption of BPA and photodegradation reaction to occurred [49,50].

As shown in Fig. 10(b), the photocatalytic degradation was found to be a pseudo-first-order kinetic process, which can be expressed by the following equation:

$$\ln\left(\frac{C}{C_0}\right) = -k_{app}t = -k_{app}t \quad (4)$$

where k_{app} is the apparent rate constant (min^{-1}), C is the concentration of pollutants (mg L^{-1}) at a specific time t is the reaction time (min), and C_0 is the initial concentration of contaminants (mg L^{-1}). The value of rate constant k_{app} is equal to the corresponding slope of the fitting line kinetics of the disappearance of BPA degradation as shown in Fig. 10(c). The improvement of reaction rate constants improvement of BTCPM g-C₃N₄ (H-0.8) was 19.26 folds as compared to the pristine g-C₃N₄. The highest in reaction rate constants value of $8.86 \times 10^{-3} \text{ min}^{-1}$ in degradation of BPA for sample BTCPM g-C₃N₄ (H-0.8) contributed to the appropriate and optimal band gap value and carbon doping contents. This characteristic leading the increased light absorption intensity and the extensive light absorption range promoted the efficient visible light harvest of BTCPM g-C₃N₄ (H-0.8). Furthermore, the carbon doping would support excellent, efficient charge carrier separation, and electron conductivity thus reduced the recombination of photo-generated electron-hole pairs.

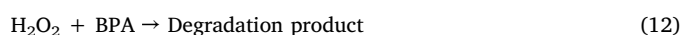
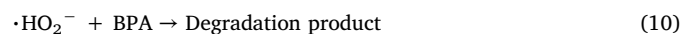
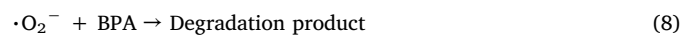
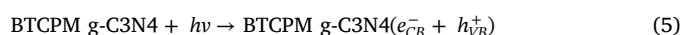
The stability and reusability of a photocatalyst is an essential parameter for practical applications. Here, we also elucidated the stability and reusability of BTCPM g-C₃N₄ (H-0.8) by collecting the remaining photocatalyst powders after photocatalytic degradation of BPA in suspension by centrifugation and followed by distilled water cleaning. As depicted in Fig. S2(a), after five successive runs with each reaction lasting for 270 min, the photodegradation of BPA by BTCPM g-C₃N₄ (H-0.8) photocatalyst could be primarily maintained. Furthermore, the FESEM image after photodegradation reaction shows there is no significant changes can be seen on the structure and shape except slight detachments of small g-C₃N₄ particles from the micro-tubular structure [Fig. S2(b)]. Nevertheless, the overall findings indicated that the BTCPM g-C₃N₄ (H-0.8) photocatalyst exhibited good photocatalytic stability and reusability.

The comparison on the photocatalytic performance of BTCPM g-C₃N₄ (H-0.8) with previously reported g-C₃N₄ with different doping element (metal and non-metal) under visible light irradiation was tabulated in Table 2. It was found that the prepared BTCPM g-C₃N₄ (H-0.8) also performed, comparable, and exhibited superior photocatalytic capability for organic contaminants under visible light irradiation. In comparison with same model pollutants (BPA), the photocatalytic efficiency of BTCPM g-C₃N₄ (H-0.8) exhibited slightly lower than sample Pd/mpg-C₃N₄ [51] and OA-g-C₃N₄ [52]. The slight variation in the data between these studies might be due to the difference in parameter used such as the type of dopant, photocatalyst dosage, light source, type of model pollutant as well as its initial concentration. Even though Pd/mpg-C₃N₄ possessed the highest reaction rate constant, the utilisation Pd as a dopant was somewhat costly to be used for industry application. For the worse scenario, it also might be leached and caused the acute aquatic toxicity as they might be reacted with other constituents such as

chloride, thus promotes secondary water pollution.

The mechanism of photocatalysis was investigated by species trapping experiments to determine the primary active species generated during the photocatalytic process under BTCPMS g-C₃N₄ system. The 1 mmol of isopropyl alcohol (IPA), 1 mmol of ammonium oxalate (AO) and 1 mmol of 1,4-benzoquinone (BQ) was added in the reaction system as the hydroxyl radical ($\cdot\text{OH}$), hole (h^+) and superoxide radical ($\cdot\text{O}_2^-$) scavenger, respectively. The comparative experiment with no scavenger was also performed under identical conditions. As shown in Fig. 10(d), the photocatalytic degradation of BPA was not affected by the addition of isopropyl alcohol indicating that the mechanism is not dominating by hydroxyl radicals ($\cdot\text{OH}$) species. On the other hand, drastically reduced in the percentage degradation of BPA was observed by the addition of BQ and AO indicating that the both of hole (h^+) and superoxide radical ($\cdot\text{O}_2^-$) are responsible for being dominant reactive species during the photocatalytic degradation of BPA.

By the experimental results above, a plausible visible light photocatalytic mechanism over BTCPM g-C₃N₄ samples was proposed, as shown in Fig. 11. Firstly, the BTCPM g-C₃N₄ absorbed the photon energy caused the electron excitation from VB to CB and leaving the positive holes at the VB (Eq. 5). The calculated VB and CB positions of BTCPM g-C₃N₄ are +1.37 V and -0.91 V vs NHE, respectively. The VB position of BTCPM g-C₃N₄ is less positive than the standard redox potential of ($\text{OH}^-/\cdot\text{OH} = +1.99 \text{ eV}$), which unable to generate the hydroxyl radicals ($\cdot\text{OH}$) species for BPA degradation. However, the photogenerated holes at the VB which possessed the high oxidative potential would allow direct oxidation of BPA and degraded them simultaneously (Eq. (6)) [57,58]. A previous study suggested that the direct hole oxidation is easily initiated when the adsorption of the photocatalysts is enough, and the concentrations of pollutants on photocatalyst surface is relatively high [54]. The increased adsorption of BPA due to strong $\pi-\pi$ interactions and the higher surface area which can be led to the higher photodegradation activity of the BTCPM g-C₃N₄ (H-0.8).



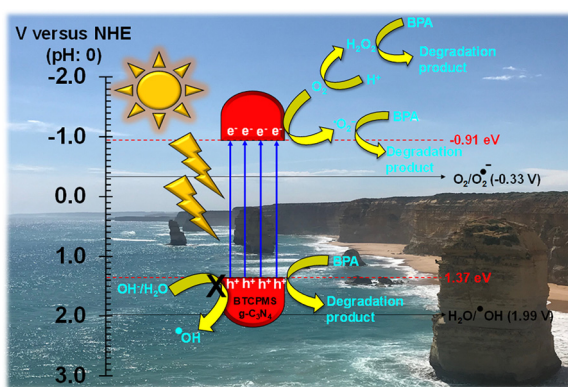
On the other hand, the CB position of BTCPM g-C₃N₄ is more negative than the reduction potential of ($\text{O}_2/\cdot\text{O}_2^- = -0.33 \text{ eV}$ vs NHE). Therefore, the photogenerated electrons BTCPMS g-C₃N₄ (e_{CB}^-) is able to reduce the molecular oxygen (O_2) into superoxide radicals ($\cdot\text{O}_2^-$) (Eq. (7)), which later degraded the organic pollutant (Eq. (8)) [59]. In the meantime, the produce superoxide radicals ($\cdot\text{O}_2^-$) also might react with H^+ to form $\cdot\text{HO}_2^-$ and H_2O_2 (Eqs. (9) & (11)) which has capability to degrade BPA (Eqs. (10) & (12)). It is reported that superoxide radicals, such as $\cdot\text{O}_2^-$ and $\cdot\text{HO}_2^-$, were very active radicals for the ring cleavage of aromatic compounds [51]. The overall separation and transfer of photogenerated electron-hole pairs in BTCPM g-C₃N₄ system and photodegradation of BPA under visible light irradiation is schematically presented in Fig. 11.

4. Conclusion

In summary, for the first time, we have successfully developed a facile method to prepare a microtubular carbon doped g-C₃N₄ inspired

Table 2Comparison of photocatalytic performance of BTCPM g-C₃N₄ (H-0.8) with another related reported doped g-C₃N₄ under visible light irradiation.

Photocatalyst	Doping element	Photocatalyst dosage (mg)	Light source	Model pollutant	Initial concentration	Photocatalytic efficiency	Ref.
C-C ₃ N ₄ granules	C	40	Sunlight irradiation	Tetracycline	50 mg/L	~ 95 %	[35]
C- g-C ₃ N ₄	C	100	300 W, Xenon	RhB	5 mg/L	~ 70 %, $36.2 \times 10^{-3} \text{ min}^{-1}$	[53]
OA-g-C ₃ N ₄	O	20	500 W, Xenon	BPA	15 mg/L	100 %, $(0.098 \text{ mmol gcat}^{-1} \text{ h}^{-1})$	[52]
O-g-C ₃ N ₄	O	80	500 W, Halogen	MB	5 mg/L	~ 80 %	[38]
PUOCNs	O	10	300 W, Xenon	MO	10 mg/L	~ 60.82 %	[54]
PSCN ₁₀	P, S	250	300 W, Xenon	MB	$4 \times 10^{-6} \text{ M}$	100 %, $48.0 \times 10^{-3} \text{ min}^{-1}$	[55]
K(0.05)-CN	K	50	250 W high-pressure sodium lamp	RhB	10 mg/L	~ 70 %, $11 \times 10^{-3} \text{ min}^{-1}$	[34]
Na(0.05)-CN	Na	50	250 W high-pressure sodium lamp	RhB	10 mg/L	~ 50 %, $6.4 \times 10^{-3} \text{ min}^{-1}$	[25]
Pd/mpg-C ₃ N ₄	Pd	25	350 W, Xenon	BPA	20 mg/L	100 %, $10.0 \times 10^{-3} \text{ min}^{-1}$	[51]
Cu/mpg-C ₃ N ₄	Cu	50	350 W, tungsten lamp	MO	10 mg/L	90.2 %	[56]
BTCPMS g-C ₃ N ₄ (H-0.8)	C	50	300 W, Xenon	BPA	10 mg/L	91.0%, $8.86 \times 10^{-3} \text{ min}^{-1}$	This study

**Fig. 11.** Schematic diagram for the separation and transfer of photogenerated electron-hole pairs in BTCPM g-C₃N₄ system and photodegradation of BPA under visible light irradiation.

by renewable kapok fibre as bio-templates. The OH-rich treated kapok fibre (t-KF) induced more urea interaction to be impregnated on the surface of t-KF. Furthermore, our findings indicate that the use of t-KF urea does not only function as bio-templates but also is responsible for in-situ carbon doping in g-C₃N₄ structure confirmed by XPS analysis. Moreover, the use of hydrothermal impregnation can be considered as a promising strategy for the well-constructed and more efficient carbon doping in g-C₃N₄. The carbon doping concentration can be easily tuned by varying the t-KF loading as in-situ carbon sources which later promotes the more appropriate band gap structures with excellent charge carrier separation. Also, the proper carbon doping concentration supports the enhancement of photocatalytic activity. The significantly high photocatalytic activity of BTCPMS g-C₃N₄ due to their unique structural and optical properties. However, the capacity of the resultant BTCPMS g-C₃N₄ in treating other organic pollutants and its degradation mechanism, as well as the kinetic study under various operating parameter, can be considered for future research. It is imperative to emphasise that the preparation of BTCPMS g-C₃N₄ photocatalyst in this study offers an economical, facile, and green approach for the development of high-performance visible light driven photocatalysts. Due to its controllable synthesis method and tuneable band gap structure and electronic properties, the versatility of prepared photocatalyst to be used in various application such as water splitting, CO₂ photoreduction, electronic material and fuel cell application also can be further explored.

Acknowledgements

The authors would also like to acknowledge the financial support Ministry of Higher Education of Malaysia under Fundamental Research Grant Scheme (FRGS/1/2017/TK10/UKM/01/3) The authors would also like to acknowledge technical and management support from Centre for Research and Instrumentation (CRIM) from Universiti Kebangsaan Malaysia. The first author also would like to thank Universiti Kebangsaan Malaysia for PhD scholarship award under the Skim Zamalah Yayasan Canselor 2016.

Appendix A. Supplementary data

Supplementary material related to this article can be found, in the online version, at doi:<https://doi.org/10.1016/j.apcatb.2018.05.037>.

References

- [1] Q. Zhang, J. Deng, Z. Xu, M. Chaker, D. Ma, High-efficiency broadband C₃N₄ photocatalysts: synergistic effects from upconversion and plasmons, *ACS Catal.* 7 (2017) 6225–6234.
- [2] L. Jiang, X. Yuan, Y. Pan, J. Liang, G. Zeng, Z. Wu, H. Wang, Doping of graphitic carbon nitride for photocatalysis: a review, *Appl. Catal. B Environ.* 217 (2017) 388–406.
- [3] Q. Zheng, D.P. Durkin, J.E. Elenewski, Y. Sun, N.A. Banek, L. Hua, H. Chen, M.J. Wagner, W. Zhang, D. Shuai, Visible-light-responsive graphitic carbon nitride: rational design and photocatalytic applications for water treatment, *Environ. Sci. Technol.* 50 (2016) 12938–12948.
- [4] M.A. Mohamed, W.N.W. Salleh, J. Jaafar, A.F. Ismail, N.A.M. Nor, Photodegradation of phenol by N-Doped TiO₂ anatase/rutile nanorods assembled microsphere under UV and visible light irradiation, *Mater. Chem. Phys.* 162 (2015) 113–123.
- [5] J. Barrio, L. Lin, X. Wang, M. Shalom, Design of a unique energy-band structure and morphology in a carbon nitride photocatalyst for improved charge separation and hydrogen production, *ACS Sustainable Chem. Eng.* 6 (2018) 519–530.
- [6] X. Li, K. Pan, Y. Qu, G. Wang, One-dimension carbon self-doping g-C₃N₄ nanotubes: synthesis and application in dye-sensitized solar cells, *Nano Res.* 11 (2018) 1322–1330.
- [7] Q.Y. Shan, B. Guan, S.J. Zhu, H.J. Zhang, Y.X. Zhang, Facile synthesis of carbon-doped graphitic C₃N₄@MnO₂ with enhanced electrochemical performance, *RSC Adv.* 6 (2016) 83209–83216.
- [8] W. Xu, B. Mu, A. Wang, Three-dimensional hollow microtubular carbonized kapok fiber/cobalt-nickel binary oxide composites for high-performance electrode materials of supercapacitors, *Electrochim. Acta* 224 (2017) 113–124.
- [9] W. Xu, B. Mu, A. Wang, Facile fabrication of well-defined microtubular carbonized kapok fiber/NiO composites as electrode material for supercapacitor, *Electrochim. Acta* 194 (2016) 84–94.
- [10] B. Mu, W. Zhang, W. Xu, A. Wang, Hollowed-out tubular carbon@MnO₂ hybrid composites with controlled morphology derived from kapok fibers for supercapacitor electrode materials, *Electrochim. Acta* 178 (2015) 709–720.
- [11] W. Xu, B. Mu, W. Zhang, A. Wang, Facile hydrothermal synthesis of tubular kapok fiber/MnO₂ composites and application in supercapacitors, *RSC Adv.* 5 (2015) 64065–64075.
- [12] H. Li, J. Li, C. Xu, P. Yang, D.H.L. Ng, P. Song, M. Zuo, Hierarchically porous MoS₂/CoAl-LDH/HCF with synergistic adsorption-photocatalytic performance under

- visible light irradiation, *J. Alloys Compd.* 698 (2017) 852–862.
- [13] E.M. Jin, J.-Y. Park, H.-B. Gu, S.M. Jeong, Synthesis of SnO_2 hollow fiber using kapok biotemplate for application in dye-sensitized solar cells, *Mater. Lett.* 159 (2015) 321–324.
 - [14] M.A. Mohamed, M. Abd Mutalib, Z.A. Mohd Hir, M.F.M. Zain, A.B. Mohamad, L. Jeffery Minggu, N.A. Awang, W.N.W. Salleh, An overview on cellulose-based material in tailoring bio-hybrid nanostructured photocatalysts for water treatment and renewable energy applications, *Int. J. Biol. Macromol.* 103 (2017) 1232–1256.
 - [15] M.A. Mohamed, W.N.W. Salleh, J. Jaafar, Z.A. Mohd Hir, M.S. Rosmi, M. Abd, A.F. Mutalib, M. Ismail, Tanemura, Regenerated cellulose membrane as bio-template for in-situ growth of visible-light driven C-modified mesoporous titania, *Carbohydr. Polym.* 146 (2016) 166–173.
 - [16] X. Tao, W. Chai, F. Xu, J. Luo, H. Xiao, C. Liang, Y. Gan, H. Huang, Y. Xia, W. Zhang, Bio-templated fabrication of highly defective carbon anchored MnO anode materials with high reversible capacity, *Electrochim. Acta* 169 (2015) 159–167.
 - [17] F. Dong, S. Guo, H. Wang, X. Li, Z. Wu, Enhancement of the visible light photocatalytic activity of C-Doped TiO_2 nanomaterials prepared by a green synthetic approach, *J. Phys. Chem. C* 115 (2011) 13285–13292.
 - [18] J. He, G. Zi, Z. Yan, Y. Li, J. Xie, D. Duan, Y. Chen, J. Wang, Biogenic C-doped titania templated by cyanobacteria for visible-light photocatalytic degradation of Rhodamine B, *J. Environ. Sci.* 26 (2014) 1195–1202.
 - [19] S. Cho, J.-W. Jang, J.S. Lee, K.-H. Lee, Carbon-doped ZnO nanostructures synthesized using vitamin C for visible light photocatalysis, *CrystEngComm* 12 (2010) 3929–3935.
 - [20] M.A. Mohamed, W.N.W. Salleh, J. Jaafar, A.F. Ismail, M. Abd Mutalib, A.B. Mohamad, M.F.M. Zain, N.A. Awang, Z.A. Mohd Hir, Physicochemical characterization of cellulose nanocrystal and nanoporous self-assembled CNC membrane derived from Ceiba pentandra, *Carbohydr. Polym.* 157 (2017) 1892–1902.
 - [21] M.A. Mohamed, J. Jaafar, M.F.M. Zain, L.J. Minggu, M.B. Kassim, M.S. Rosmi, N.H. Alias, N.A. Mohamad Nor, W.N.W. Salleh, M.H.D. Othman, In-depth understanding of core-shell nanoarchitecture evolution of $\text{g-C}_3\text{N}_4/\text{C}$, N co-doped anatase/rutile: efficient charge separation and enhanced visible-light photocatalytic performance, *Appl. Surf. Sci.* 436 (2018) 302–318.
 - [22] M.A. Mohamed, J. Jaafar, M.F.M. Zain, L.J. Minggu, M.B. Kassim, M.N.I. Salehmin, M.S. Rosmi, W.N.W. Salleh, M.H.D. Othman, Concurrent growth, structural and photocatalytic properties of hybridized C, N co-doped TiO_2 mixed phase over $\text{g-C}_3\text{N}_4$ nanostructured, *Scr. Mater.* 142 (2018) 143–147.
 - [23] A. Thomas, A. Fischer, F. Goettmann, M. Antonietti, J.-O. Müller, R. Schlögl, J.M. Carlsson, Graphitic carbon nitride materials: variation of structure and morphology and their use as metal-free catalysts, *J. Mater. Chem.* 18 (2008) 4893–4908.
 - [24] F. Dong, Y. Sun, L. Wu, M. Fu, Z. Wu, Facile transformation of low cost thiourea into nitrogen-rich graphitic carbon nitride nanocatalyst with high visible light photocatalytic performance, *Catal. Sci. Technol.* 2 (2012) 1332–1335.
 - [25] J. Zhang, S. Hu, Y. Wang, A convenient method to prepare a novel alkali metal sodium doped carbon nitride photocatalyst with a tunable band structure, *RSC Adv.* 4 (2014) 62912–62919.
 - [26] J. Fu, B. Zhu, C. Jiang, B. Cheng, W. You, J. Yu, Hierarchical porous O-doped $\text{g-C}_3\text{N}_4$ with enhanced photocatalytic CO_2 reduction activity, *Small* 13 (2017) 1603938.
 - [27] N. Sagara, S. Kamimura, T. Tsubota, T. Ohno, Photoelectrochemical CO_2 reduction by a p-type boron-doped $\text{g-C}_3\text{N}_4$ electrode under visible light, *Appl. Catal. B Environ.* 192 (2016) 193–198.
 - [28] Y. Liu, P. Liu, C. Sun, T. Wang, K. Tao, D. Gao, P dopants induced ferromagnetism in $\text{g-C}_3\text{N}_4$ nanosheets: experiments and calculations, *Appl. Phys. Lett.* 110 (2017) 2–7.
 - [29] Z. Tong, D. Yang, Y. Sun, Y. Nan, Z. Jiang, Tubular $\text{g-C}_3\text{N}_4$ isotype heterojunction: enhanced visible-light photocatalytic activity through cooperative manipulation of oriented electron and hole transfer, *Small* 12 (2016) 4093–4101.
 - [30] H. Liu, Z. Xu, Z. Zhang, D. Ao, Highly efficient photocatalytic H_2 evolution from water over CdLa_2S_4 /mesoporous $\text{g-C}_3\text{N}_4$ hybrids under visible light irradiation, *Appl. Catal. B Environ.* 192 (2016) 234–241.
 - [31] C. Han, Y. Wang, Y. Lei, B. Wang, N. Wu, Q. Shi, Q. Li, In situ synthesis of graphitic- C_3N_4 nanosheet hybridized N-doped TiO_2 nanofibers for efficient photocatalytic H_2 production and degradation, *Nano Res.* 8 (2015) 1199–1209.
 - [32] H. Bin Fang, X.H. Zhang, J. Wu, N. Li, Y.Z. Zheng, X. Tao, Fragmented phosphorus-doped graphitic carbon nitride nanoflakes with broad sub-bandgap absorption for highly efficient visible-light photocatalytic hydrogen evolution, *Appl. Catal. B Environ.* 225 (2018) 397–405.
 - [33] J.Y. Su, P. Geng, X.Y. Li, Q.D. Zhao, X. Quan, G.H. Chen, Novel phosphorus doped carbon nitride modified TiO_2 nanotube arrays with improved photoelectrochemical performance, *Nanoscale*. 7 (2015) 16282–16289.
 - [34] S. Hu, F. Li, Z. Fan, F. Wang, Y. Zhao, Z. Lv, Band gap-tunable potassium doped graphitic carbon nitride with enhanced mineralization ability, *Dalt. Trans.* 44 (2015) 1084–1092.
 - [35] S. Panneri, P. Ganguly, M. Mohan, B.N. Nair, A.A.P. Mohamed, K.G. Warriar, U.S. Hareesh, Photoregenerable, bifunctional granules of carbon-doped $\text{g-C}_3\text{N}_4$ as adsorptive photocatalyst for the efficient removal of tetracycline antibiotic, *ACS Sustain. Chem. Eng.* 5 (2017) 1610–1618.
 - [36] J. Liu, T. Zhang, Z. Wang, G. Dawson, W. Chen, Simple pyrolysis of urea into graphitic carbon nitride with recyclable adsorption and photocatalytic activity, *J. Mater. Chem.* 21 (2011) 14398–14401.
 - [37] M. Zhang, Y. Duan, H. Jia, F. Wang, L. Wang, Z. Su, C. Wang, Defective graphitic carbon nitride synthesized by controllable co-polymerization with enhanced visible light photocatalytic hydrogen evolution, *Catal. Sci. Technol.* 7 (2017) 452–458.
 - [38] J. Li, B. Shen, Z. Hong, B. Lin, B. Gao, Y. Chen, A facile approach to synthesize novel oxygen-doped $\text{g-C}_3\text{N}_4$ with superior visible-light photoreactivity, *Chem. Commun.* 48 (2012) 12017–12019.
 - [39] H. Yang, R. Yan, H. Chen, D.H. Lee, C. Zheng, Characteristics of hemicellulose, cellulose and lignin pyrolysis, *Fuel*. 86 (2007) 1781–1788.
 - [40] A. Wang, C. Wang, L. Fu, W. Wong-Ng, Y. Lan, Recent advances of graphitic carbon nitride-based structures and applications in catalyst, sensing, imaging, and LEDs, *Nano-Micro Lett.* 9 (2017) 47.
 - [41] X. Wang, S. Blechert, M. Antonietti, Polymeric graphitic carbon nitride for heterogeneous photocatalysis, *ACS Catal.* 2 (2012) 1596–1606.
 - [42] Z. Jiang, D. Liu, D. Jiang, W. Wei, K. Qian, M. Chen, J. Xie, Bamboo leaf-assisted formation of carbon/nitrogen co-doped anatase TiO_2 modified with silver and graphitic carbon nitride: novel and green synthesis and cooperative photocatalytic activity, *Dalton Trans.* 43 (2014) 13792–13802.
 - [43] Y. Hong, Z. Fang, B. Yin, B. Luo, Y. Zhao, W. Shi, C. Li, A visible-light-driven heterojunction for enhanced photocatalytic water splitting over Ta_2O_5 modified $\text{g-C}_3\text{N}_4$ photocatalyst, *Int. J. Hydrogen Energy*. (2016) 6–13.
 - [44] S. Wang, D. Li, C. Sun, S. Yang, Y. Guan, H. He, Synthesis and characterization of $\text{g-C}_3\text{N}_4/\text{Ag}_3\text{VO}_4$ composites with significantly enhanced visible-light photocatalytic activity for triphenylmethane dye degradation, *Appl. Catal. B Environ.* 144 (2014) 885–892.
 - [45] M. Yan, Y. Hua, F. Zhu, L. Sun, W. Gu, W. Shi, Constructing nitrogen doped graphene quantum dots- $\text{ZnNb}_2\text{O}_6/\text{g-C}_3\text{N}_4$ catalysts for hydrogen production under visible light, *Appl. Catal. B Environ.* 206 (2017) 531–537.
 - [46] Y. Wu, L. Tao, J. Zhao, X. Yue, W. Deng, Y. Li, C. Wang, $\text{TiO}_2/\text{g-C}_3\text{N}_4$ nanosheets hybrid photocatalyst with enhanced photocatalytic activity under visible light irradiation, *Res. Chem. Intermed.* 42 (2015) 3609–3624.
 - [47] S. Guo, Z. Deng, M. Li, B. Jiang, C. Tian, Q. Pan, H. Fu, Phosphorus-doped carbon nitride tubes with a layered micro-nanostructure for enhanced visible-light photocatalytic hydrogen evolution, *Angew. Chem. – Int. Ed.* 55 (2016) 1830–1834.
 - [48] J. Wen, J. Xie, X. Chen, X. Li, A review on $\text{g-C}_3\text{N}_4$ -based photocatalysts, *Appl. Surf. Sci.* 391 (2017) 72–123.
 - [49] M.A. Mohamed, W.N. Wan Salleh, J. Jaafar, M.S. Rosmi, Z.A. Mohd. Hir, M. Abd. Mutalib, A.F. Ismail, M. Tanemura, Carbon as amorphous shell and interstitial dopant in mesoporous rutile TiO_2 : bio-template assisted sol-gel synthesis and photocatalytic activity, *Appl. Surf. Sci.* 393 (2017) 46–59.
 - [50] Z. Mohd Hir, A. Abdullah, Z. Zainal, H. Lim, Photoactive hybrid film photocatalyst of polyethersulfone- ZnO for the degradation of methyl orange dye: kinetic study and operational parameters, *Catalysts* 7 (2017) 313.
 - [51] C. Chang, Y. Fu, M. Hu, C. Wang, G. Shan, L. Zhu, Photodegradation of bisphenol A by highly stable palladium-doped mesoporous graphite carbon nitride ($\text{Pd}/\text{mpg-C}_3\text{N}_4$) under simulated solar light irradiation, *Appl. Catal. B Environ.* 143 (2013) 553–560.
 - [52] P. Qiu, C. Xu, H. Chen, F. Jiang, X. Wang, R. Lu, X. Zhang, One step synthesis of oxygen doped porous graphitic carbon nitride with remarkable improvement of photo-oxidation activity: role of oxygen on visible light photocatalytic activity, *Appl. Catal. B Environ.* 206 (2017) 319–327.
 - [53] D.A. Links, Carbon self-doping induced high electronic conductivity and photo-reactivity of $\text{g-C}_3\text{N}_4$, *Chem. Commun.* 48 (2012) 6178–6180.
 - [54] X. She, L. Liu, H. Ji, Z. Mo, Y. Li, L. Huang, D. Du, H. Xu, H. Li, Template-free synthesis of 2D porous ultrathin nonmetal-doped $\text{g-C}_3\text{N}_4$ nanosheets with highly efficient photocatalytic H_2 evolution from water under visible light, *Appl. Catal. B Environ.* 187 (2016) 144–153.
 - [55] C. Hu, W.-Z. Hung, M.-S. Wang, P.-J. Lu, Phosphorus and sulfur codoped $\text{g-C}_3\text{N}_4$ as an efficient metal-free photocatalyst, *Carbon* 127 (2018) 374–383.
 - [56] S. Le, T. Jiang, Q. Zhao, X. Liu, Y. Li, B. Fang, M. Gong, Cu-doped mesoporous graphitic carbon nitride for enhanced visible-light driven photocatalysis, *RSC Adv.* 6 (2016) 38811–38819.
 - [57] M. Khatamian, Z. Alaji, Efficient adsorption-photodegradation of 4-nitrophenol in aqueous solution by using $\text{ZnO}/\text{HZSM-5}$ nanocomposites, *Desalination* 286 (2012) 248–253.
 - [58] Z. Jiang, C. Zhu, W. Wan, K. Qian, J. Xie, Constructing graphite-like carbon nitride modified hierarchical yolk-shell TiO_2 spheres for water pollution treatment and hydrogen production, *J. Mater. Chem. A* 4 (2016) 1806–1818.
 - [59] M. Mahajan, G. Singla, K. Singh, O.P. Pandey, Synthesis of grape-like carbon nanospheres and their application as photocatalyst and electrocatalyst, *J. Solid State Chem.* 232 (2015) 108–117.